HiSST: International Conference on
High-Speed Vehicle Science Technology

26–29 November 2018, Moscow, Russia

Mixing Characteristics in a Hypersonic Flow around a Transpiration Cooled Flat Plate Model

Tobias Hermann[1], *Hassan Saad Ifti*[2], *Matthew McGilvray*[3], *Luke Doherty*[4], *Rowland Penty Geraets*[5]

Abstract

This paper presents transpiration cooling experiments conducted in the Oxford High Density Tunnel. The flow structure and mixing phenomena between the injected coolant gas and the hypersonic free stream are investigated. A flat plate model is used which is equipped with a gas injection system, four surface mounted heat flux gauges and three surface pressure sensors located downstream of the injection point. Mass injection is realized through a porous ceramic material, and alternatively through a series of slots. Spatially and temporally resolved film effectiveness downstream of the injection point is measured with fast response pressure sensitive paint. The flowfield is visualised by a Z-type Schlieren imaging system. Results show a significant influence of injection on the boundary layer thickness through the additional coolant gas. High blowing ratios can lead to early transition which increases coolant-external flow mixing and leads to a lower film effectiveness. Transpiration cooling requires approximately two orders of magnitude lower blowing ratios to achieve a similar film coverage as in the case of the injection through slots. The film effectiveness increases with an increasing blowing ratio for locations close to the injection point. However, a lower blowing ratio results in a more stable film for locations further downstream.

Keywords: *Transpiration cooling, flat plate, Ludwieg tube, Schlieren, pressure sensitive paint*

Nomenclature

Latin

A – Polynomial coefficient
c_p – Specific heat capacity, $\mathrm{J\,kg^{-1}\,K^{-1}}$
f – Focal length, m
F – Blowing ratio
FN – F-number
I – Intensity, counts
i – Iteration parameter
j – Iteration parameter
k – Thermal conductivity, $\mathrm{W\,m^{-1}\,K^{-1}}$
K_D – Darcy coefficient, $\mathrm{m^2}$
K_F – Forchheimer coefficient, m
L – Material thickness, m
M – Mach number
p – Pressure, Pa
Re_x – Reynolds number at location x
T – Temperature, K
u – velocity, $\mathrm{m\,s^{-1}}$
V – Voltage, V
W – Molecular weight, u
x – Distance from model tip, m

Greek

α_R – Coefficient of resistance, $\mathrm{K^{-1}}$
ε – Emissivity

[1]*Post-doctoral Research Assistant, Hypersonics group, Oxford Thermofluids Institute, Osney Mead, Oxford OX2 0ES, United Kingdom, tobias.hermann@eng.ox.ac.uk*
[2]*DPhil student, Hypersonics group, Oxford Thermofluids Institute, Osney Mead, Oxford OX2 0ES, United Kingdom, saad.ifti@eng.ox.ac.uk*
[3]*Associate Professor, Hypersonics group, Oxford Thermofluids Institute, Osney Mead, Oxford OX2 0ES, United Kingdom, matthew.mcgilvray@eng.ox.ac.uk*
[4]*Senior Research Associate, Hypersonics group, Oxford Thermofluids Institute, Osney Mead, Oxford OX2 0ES, United Kingdom, luke.doherty@eng.ox.ac.uk*
[5]*DPhil student, Hypersonics group, Oxford Thermofluids Institute, Osney Mead, Oxford OX2 0ES, United Kingdom, rowland.pentygeraets@balliol.ox.ac.uk*

Copyright © 2018 by the author(s)

λ – Thermal conductivity, $\mathrm{W\,m^{-1}\,K^{-1}}$
ϕ – Porosity
ρ – Density, $\mathrm{kg\,m^{-3}}$
Subscripts
∞ – Free stream, boundary layer edge
0 – Total condition
BG – Background
c – coolant gas
fill – Initial filling condition of Ludwieg tube
initial – test section condition immediately before an experiment
inject – Injection condition in plenum
injector – At injector location
or – Original measurement
O2 – Molecular Oxygen
ref – Reference condition
stag – Stagnation condition

1. Introduction

Hypersonic vehicles are exposed to large heat loads that necessitate some kind of thermal management system in order to protect the crew or payload [1]. Depending on the vehicle's trajectory, different types of heat shields are used to mitigate, absorb, and re-radiate the heat load and hence keep the temperature of the sub-structure below critical values. Transpiration cooling is an active cooling technique that aims to enable re-usable thermal protection systems for flow conditions where the performance of current materials does not suffice [2]. The active cooling technique is intended to allow re-usability by keeping the material below critical temperatures, e. g. oxidation, sublimation, or melting [3, 4]. It could also enable a higher performance of the thermal protection system compared to current approaches, through the expense of complexity [2]. This is especially useful for hypersonic flow conditions where high heat fluxes are experienced at the vehicle surface [5, 6, 7, 8, 9, 10, 11, 12]. Coolant gas or liquid is fed through the porous heat shield which results in two cooling mechanisms: Convective heat transfer between solid and fluid phase in the porous material, and the establishment of a relatively cold coolant film at the surface which reduces boundary layer temperatures [13]. Past investigations have shown that the injection at large blowing ratios of coolant gas can lead to an earlier onset of transition to turbulence [14]. For small blowing ratios and laminar flow, excellent cooling effectiveness has been reported [15]. However, there is little knowledge about the structure of the flow field. Most investigations focused on surface temperature measurements, either highly spatially resolved with infrared imaging systems or local measurements by surface mounted thermocouples [14, 15]. Surface measurement allows for an assessment of the cooling performance, but does not provide sufficient information to analyse the mixing phenomena occurring between the hot external flow and the cool injected gas layer. Understanding the mixing behaviour enables the development of prediction tools for active cooling systems that can eventually lead to optimising the design of such heat shields. Furthermore, mixing is an important quantity for studies of porous fuel injection for supersonic combuster applications [11]. This study aims to provide additional information about the flow phenomena occurring near the injection point by using a variety of measurement techniques that assess the flow structure as well as the surface state. Pressure sensitive paint, Schlieren imaging, pressure sensors and thin film heat transfer gauges are used to achieve this. These different diagnostics enable a more in depth analysis of the flow-coolant mixing phenomena that occur due to the gas injection into the boundary layer.

2. Experimental setup

2.1. The Oxford high density tunnel

The experiments described here are conducted in the High Density Tunnel (HDT) of the Oxford Thermofluids Institute [16]. For the purpose of the current work, the facility operates as a Ludwieg tube. It consists of a 17.4 m long barrel with an internal diameter of 152.4 mm which is filled with high pressure air before each experiment. A bespoke fast-acting plug valve separates the barrel from a contoured and the facility test section. Several nozzles are available allowing tests of Mach numbers ranging between 3 and 7 (see Table 1). After opening the plug valve, the high pressure air is released into the previously evacuated nozzle and test section. This sudden event initiates expansion waves that travel upstream in the barrel and eventually reflect at the barrel rear wall. As the reflected expansion waves pass the plug valve, the total pressure in the high pressure tube is lowered and the resulting Ludwieg tube driving

Copyright © 2018 by the author(s)

conditions have a lower total pressure. This results in various steady test times (henceforth referred to as ”plateaus”) which feature successively lower total pressures. Steady state test times of each plateau are in the order of tens of milliseconds and the total number of plateaus can be adjusted by specifying the opening times of the plug valve. An example stagnation pressure trace is shown in Fig. 1 where five plateaus are indicated. Alternatively, the facility can be operated in LICH mode (light isentropic compression heating) which necessitates the addition of a piston into the high pressure barrel. All presented data of the current work has been obtained by using the Ludwieg tube mode of the facility. The test section is fitted with a traverse mechanism, allowing automatic re-orientation of an experimental model over a range of $\pm 15^{\circ}$ angle of attack and $\pm 5^{\circ}$ angle of yaw [17].

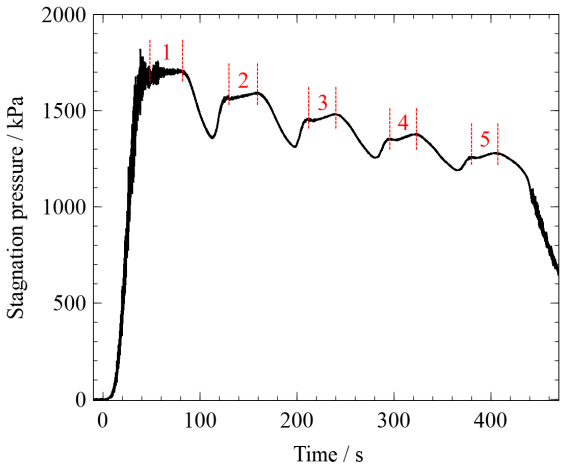


Fig 1. Example of HDT stagnation pressure in the settling chamber upstream of the nozzle throat. Red lines show the five steady test periods.

The barrel is equipped with electrical heaters that are used to elevate the temperature of the initial fill gas. This way, the total temperature of the flow can be adjusted and a wider range of Mach numbers is available since liquefaction of nitrogen after the expansion in the nozzle is prevented. High pressure air for the filling of the tube and the operation of valves is supplied by the laboratory compressed gas manifold. The facility is operated remotely via a semi-automated programmable logic circuit (PLC) that provides control over all relevant valves and is used to monitor the state of each section of the facility. An overview of the test envelope is presented in Table 1 and a more detailed description of the facility can be found in Ref. [16].

Table 1. High Density Tunnel Condition envelope [16, 17].

Property	Mach 3	Mach 4	Mach 5	Mach 6	Mach 7
Maximum total pressure / bar	30	95	100	90	90
Minimum total temperature / K	288	300	454[1]	537[1]	537[1]
Maximum unit Reynolds number 10^6/m	493	694	326	120	58

[1] Lowest total temperature run to date with this nozzle.

2.2. Test model

In the past a significant body of work has investigated transpiration cooling using flat plate models [14, 15, 19, 20, 21]. To build on this foundation, the flat plate approach is adopted in this study. The particular aim of this work is to improve the understanding of the fundamental flow dynamics without the introduction of additional complexities, such as curved or three-dimensional geometries. The employed

Copyright © 2018 by the author(s)

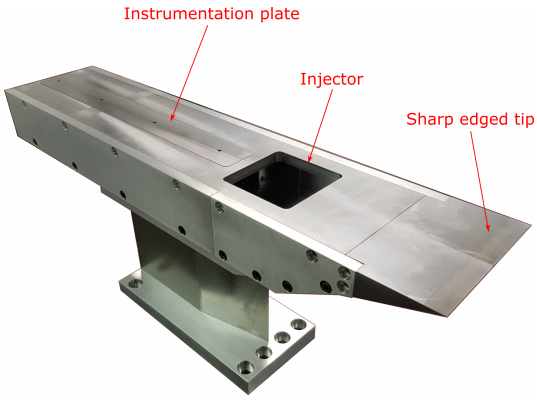


Fig 2. Flat plate test model with no injector installed.

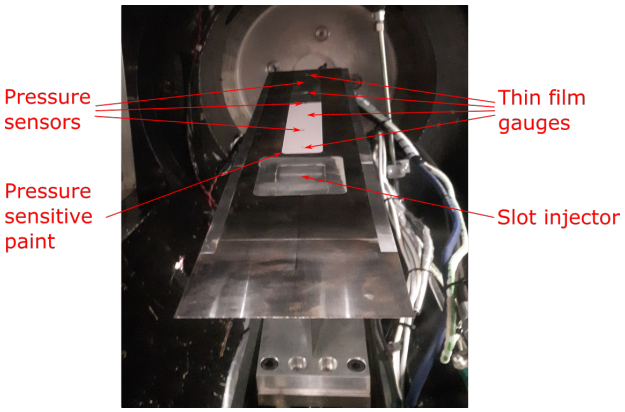


Fig 3. Flat plate test model (front view) installed in the high density tunnel.

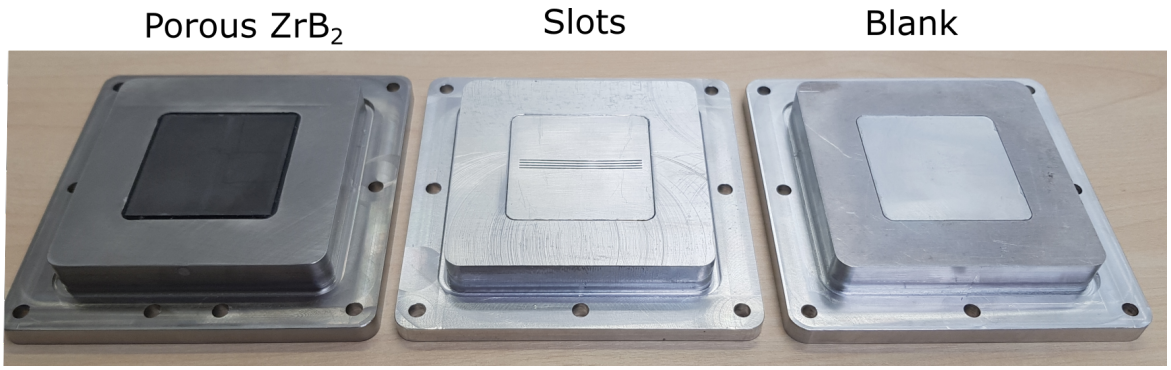


Fig 4. Injector pieces used in this work.

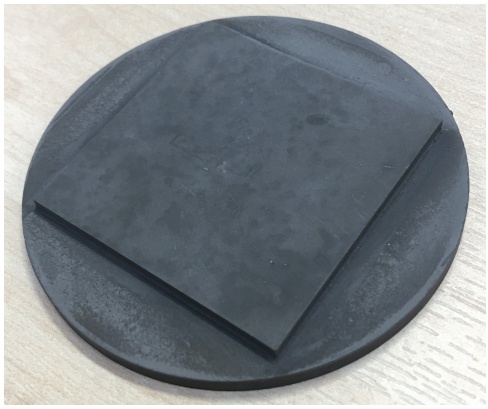


Fig 5. Machined porous ZrB_2 sample [18].

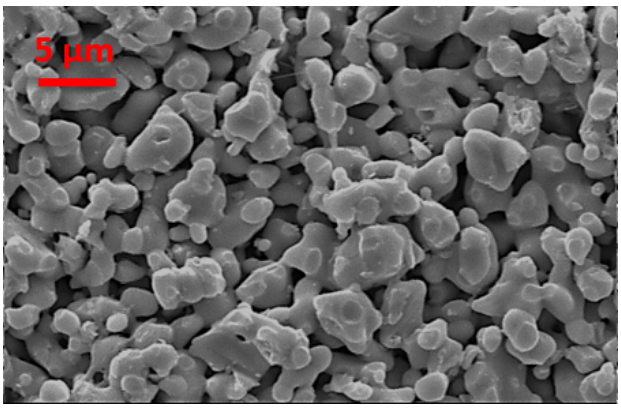


Fig 6. Micro-structure of the porous ZrB_2 sample [18].

Copyright © 2018 by the author(s)

Table 2. Material properties of the porous ZrB_2 injector [26, 18, 27] .

L	5 mm
ϕ	42 %
λ	41.4 W m^{-1} K^{-1}
c_p	437.6 J kg^{-1} K^{-1}
ρ	6080 kg m^{-3}
K_D	$3.731 \cdot 10^{-14}$ m^2
K_F	$1.538 \cdot 10^{-7}$ m
ε	0.75

model is 580 mm long and 125 mm wide. A photograph of the model is shown in Fig. 2 and the installed model in the wind tunnel is shown in Fig. 3. A 39 mm $\times$ 39 mm square geometry is used as the porous injector which is located 160 mm downstream of the sharp leading edge. The porous material used in this study is partially sintered ZrB_2, an ultra high temperature ceramic (UHTC), which is manufactured by Imperial College London and has been analysed in detail in Refs. [4, 22, 18, 23, 24, 25]. The material properties of the porous sample are summarised in Table 2. The UHTC is manufactured through partial sintering by Imperial College London and features porous channels with a length scale in the order of μm. A photograph of a machined sample and a microscopic image of the sample are shown in Figs. 5 and 6.

In addition to the porous material, an insert with a series of four slots is used. Each of the slots is 0.2 mm wide and 30 mm long and separated from one another by a distance of 1 mm. The first slot is located 177 mm from the model tip. No injection cases are conducted with a blank insert. All injector types are shown in Fig. 4. The comparison between measurements of no injection and the slotted injector is intended to provide useful data for the validation of numerical simulations of the experiments [28]. The investigated gas types are Air, N_2 and CO_2 [29, 13, 30]. N_2 has been used in many previous studies whereas CO_2 is mainly used to allow for visualisation of the film distribution through the use of Schlieren imaging. The large difference in refractive index between air and CO_2 is exploited to visualise the injected gas. The operation of the injection system is controlled by the facility PLC, ensuring correct timing of the injection in relation to onset of the hypersonic test flow. Before a test, a reservoir upstream of the plenum is filled with the coolant gas to the desired pressure. At this stage, the plenum is evacuated and is separated from the reservoir by a fast acting solenoid valve. Upon firing the facility, the solenoid valve is opened and the coolant gas expands into the plenum and subsequently through the injector piece into the hypersonic cross flow. In order to regulate the achievable pressures in the plenum, an orfice is placed in the pipework between the reservoir and the plenum. The orfice limits the mass flow rate that can enter the plenum, thus effectively reducing the plenum injection pressure. Depending on the injection condition, orfice diameters between 0.5 mm (slot injector) and 5.0 mm (porous injector) are used.

Figure 7 presents a compilation of experimental flat plate investigations from the literature [21, 19, 14, 20] and from the current experimental campaign. For the current work, the boundary layer edge Reynolds numbers at the injection location and the respective blowing ratios are based on the following models and measurements: Transient total temperature data is extracted from a measurement with an aspirated thermocouple [31]. The static temperature at the boundary layer edge is then obtained by applying an isentropic expansion and, in the case of a non-zero angle of attack, oblique shock relations. The static pressure is obtained from surface mounted pressure sensors. The boundary layer edge velocity is then calculated using the post shock Mach number and the sonic velocity based on the static temperature. The static temperature is furthermore used in Keyes' viscosity model and in the ideal gas equation which is used to determine the boundary layer edge density and hence edge mass flux [32, 33, 34]. Similarly, the measured plenum temperature and pressure are used to determine the coolant density that is injected into the cross flow. In the case of the slot injector, a chocked mass flow

Copyright © 2018 by the author(s)

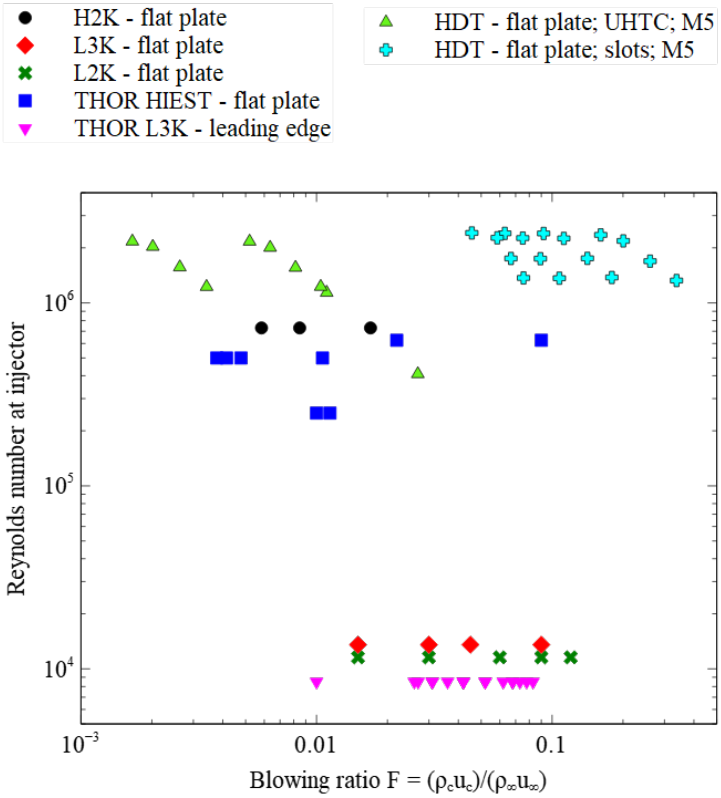


Fig 7. Overview of conditions from the literature and the current work [21, 19, 14, 20].

Table 3. Flow conditions run for this study. All parameters refer to air injection and the steady test time during the second plateau.

Condition	1	2	3
Shot number	$410-423$	$424-428, 434, 435$	$429-433$
Injector type	Slots	UHTC	UHTC
Coolant gas	Air, N_2, CO_2	Air, N_2, CO_2	Air, N_2, CO_2
Angle of attack /	0	0	0
M	5	5	5
p_{fill} / kPa	1623	1623	858
T_{fill} / K	537	537	537
$Re_{x,\,injector}$	$2.24 \cdot 10^6$	$2.04 \cdot 10^6$	$1.15 \cdot 10^6$
p_{stag} / kPa	864	864	506
[1]T_0 / K	460	460	460
[2]p_{inject} / kPa	$2.6-8.7$	$244-430$	428
[3]p_{static} / kPa	1.74	1.74	0.97
$F = (\rho_c u_c)/(\rho_\infty u_\infty)$	$0.058-0.200$	$0.0020-0.0064$	0.011

[1] Measurement by heated thin film sensors and aspirated thermocouples [31].
[2] Measurement by plenum pressure sensor.
[3] Measurement by static pressure sensor on plate surface.

Copyright © 2018 by the author(s)

is assumed and a discharge coefficient of 0.754 is used [35]. It is planned to calibrate the mass flow rate with respect to the measured plenum pressure in a post test analysis. In the case of the porous injector, the Darcy-Forchheimer equation is solved with the calibrated permeability coefficients [18]. Both mass fluxes are then used to determine the respective blowing ratio.

2.3. Diagnostics

A variety of sensor instrumentation and optical diagnostics are employed to investigate the flow phenomena occurring in the experiments. The different diagnostics and post processing steps are described in detail in the following.

2.3.1. Sensor instrumentation

The surface of the model downstream of the injector is instrumented with three Kulite XCEL-152-25A pressure transducers and four platinum thin film gauges on quartz bodies which were manufactured by the University of Queensland [36].

All measured data is acquired using a National Instruments PXIe-8135 controller with several PXIe-6368 (2 MHz/channel) and PXIe-6363 (2 MHz aggregate) cards. The data acquisition system is run using an in-house Labview code which is based on a program originally developed for the reflected shock tunnel T4 of the University of Queensland [37]. A sample rate of 1 μs is used to record all signals of the measurement which includes model and wind tunnel instrumentation. The pressure transducers allow for the measurement of the static pressure along the length of the model and the thin film gauges allow for a measurement of the local heat flux.

The gas injection plenum is equipped with a 1.5 mm diameter type K thermocouple that is used to monitor the coolant temperature before and during injection. The plenum pressure is measured using a Kulite XTEL-140M-3.5BARA transducer. All pressure signals are amplified by using a FYLDE H379TA full bridge amplifier and the thermocouple data is amplified by a FYLDE 351UA amplifier [17]. The measured data is then filtered using a moving average filter with a length of 300 μs.

A constant current of approximately 10 mA is supplied to each of the thin film gauges. As the temperature of the thin film changes during an experiment, the electrical resistance of the platinum film changes, and so the change in temperature can be measured through a change in voltage. The current is supplied, and the voltage signal is amplified, by the in-house amplifier HTA4.5. The amplifier has a gain profile which rises with frequency to reduce digitisation errors and signal to noise issues for high frequency heat flux fluctuations [38]. The amplification is conducted within the test section allowing short cable lengths and thus significantly reducing the influence of electro-magnetic noise. The measured signals must be post-processed to de-emphasise the frequency dependant gain. This so-called de-boosting is achieved through the convolution of the inverse impulse response of the amplifier with the measured signal [39].

The de-boosted voltage is converted into temperature by

$$T(t) = \frac{V(t) - V_{\text{ref}}}{\alpha_R V_{\text{ref}}} + T_{\text{ref}} \tag{1}$$

where $T(t)$ is the time dependant thin film temperature, and α_R is the coefficient of resistance with temperature. The reference voltage V_{ref} is measured at an isothermal temperature T_{ref} in-situ in the wind tunnel [40]. The coefficient of resistance with temperature is found by calibrating the thin film gauges in a hot water bath according to the work of Collins et al. [41]. The experimentally recorded temperature data is used to calculate the surface heat flux by applying the impulse response convolution approach of Oldfield [39]. The thermal product of the quartz substrate needed for this method was taken to be $\sqrt{\rho c_p k} = 1531.4\,\text{J}\,\text{m}^{-2}\,\text{K}^{-1}\,\text{s}^{-0.5}$. The impulse response of the gauges is calculated assuming heat conduction into a one-dimensional semi-infinite slab of material. This assumption is valid for very thin platinum film layers and as long as the thermal penetration depth during the test is smaller than the thickness of the substrate [42]. These assumptions apply for the short-duration experiments conducted

Copyright © 2018 by the author(s)

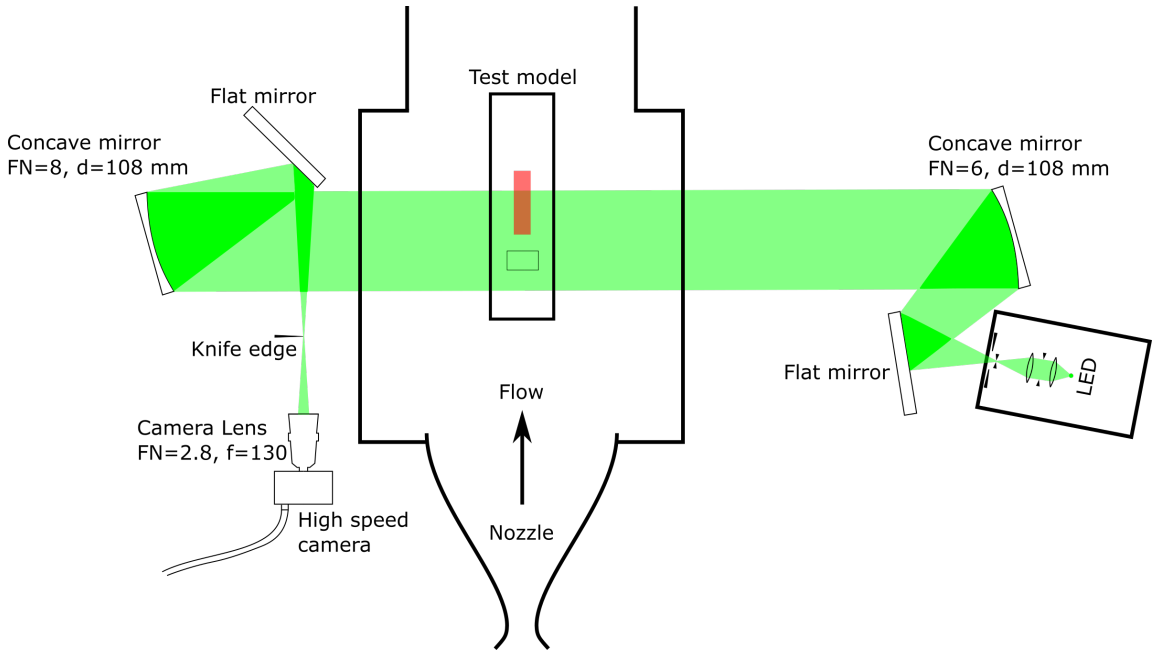


Fig 8. Plan view of the Z-type Schlieren setup with the flap plate model in the test section.

in the High Density Tunnel. The resulting heat transfer data is smoothed by a moving average filter with a length of 1 ms.

2.3.2. Schlieren imaging

A conventional Z-type Schlieren system is used to visualise the density gradients in the flowfield above the flat plate model [43]. A plan view of the optical setup is shown in Fig. 8. The light source is operated by overdriving a Luminus PT-120-TE green LED with approximately 150 A for 2.5 μs pulses with a 50 % duty-cycle. Green light is used as the camera's detector is especially sensitve to this wavelength region. The fast high current pulses are achieved using an in-house built electrical circuit which relies on storing charge in a capacitor and releasing it at the exact time of measurement acquisition. The circuit is based on the work of Willert et al. [44, 45]. Within a confined enclosure, the LED radiation is collected by an aspherical condenser lens and collimated. The collimated light is limited by an iris to set the desired solid angle (F-number) of the beam before being refocused with a magnification of 1. At the location of the image, a horizontal slit is used to cut the LED image in the horizontal, i. e. the cut-off direction [46]. This ensures a defined edge of the light source that will eventually result in a linear Schlieren intensity variation with density gradient and prevent spatial non-uniformities in the acquired image.

Two concave parabolic mirrors are used with a diameter of 108 mm. The same diameter corresponds therefore to the imaged cross section of the flow. The concave mirror on the source side features a focal length of 648 mm (FN=6) and the counterpart on the detection side features a focal length of 864 mm (FN=8). This results in a higher magnification of the LED image on the detection side which in turn allows an easier setting for the Schlieren sensitivity, i. e. the cut-off ratio at the knife edge. Approximately 75 % of the projected LED image is cut off at the knife edge. A horizontal knife edge is used to view density gradients normal to the surface of the flat plate. Furthermore, a vertical slit is used at the knife edge location which limits the horizontal extent of the LED image. This prevents astigmatism due to the relatively wide LED shape.

The Schlieren image is acquired with a Kirana 05M high speed camera at a frame rate of 50,000 Hz and shutter time of 5 μs. The camera captures 180 images at a resolution of 768 $\times$ 924 pixels with a bit depth of 10. The acquisition rate results in a total recorded time span of 3.6 ms. The camera acquisition

Copyright © 2018 by the author(s)

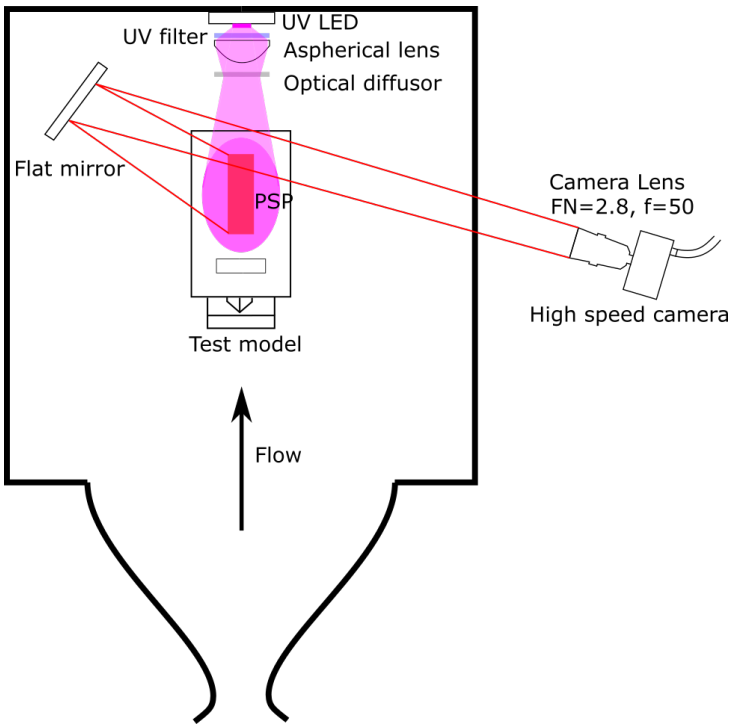


Fig 9. Pressure sensitive paint setup.

and light source are triggered such that the recording interval occurs during the second steady state plateau of the facility nozzle supply pressure trace (1).

The captured images are post processed by subtracting a background image where no flow is present [45, 47]. Subsequently, the background image is further used to scale the intensity of the acquired high speed video which removes the majority of the spatial non-uniformity of the light source. The intensity of pixel i, j is calculated via

$$I_{\text{Schlieren}}(i,j) = \frac{I_{\text{or}}(i,j) - I_{\text{BG}}(i,j)}{I_{\text{BG}}(i,j)} \tag{2}$$

with the original acquisition I_{or} and the background image I_{BG}. Finally, the contrast of the processed video file is adjusted to visualise the flow features more clearly.

2.3.3. Pressure sensitive paint

The film effectiveness downstream of the injection point is assessed by using fast-response pressure sensitive paint (PSP). The paint used in this work is ISSI FP-100 which is sensitive to the surface oxygen partial pressure and features a response time below 100 μs. This fast response is achieved by creating a porous sublayer on the model surface before applying the paint. The porous sublayer provides significantly more surface area for the paint to interact with oxygen molecules in the flow, increasing the response time. The overall setup within the wind tunnel is shown in Fig. 9.

The paint is excited by ultraviolet radiation from a Luminus PT-120-TE UV high power LED that is continuously driven with a current of 20 A. The LED is mounted directly above the model within the test section. Before an experiment, the LED is turned on for a time period of approximately 2 minutes in order to reach thermal equilibrium and improve repeatability between tests. The emitted radiation is filtered by a UV bandpass filter with a central wavelength of 390 nm and a full width at half maximum of 125 nm. The radiation is subsequently collimated with an aspherical lens and then evenly re-emitted by using an optical diffusor. This way, the majority of the UV radiation is distributed over the PSP coated surface area.

Copyright © 2018 by the author(s)

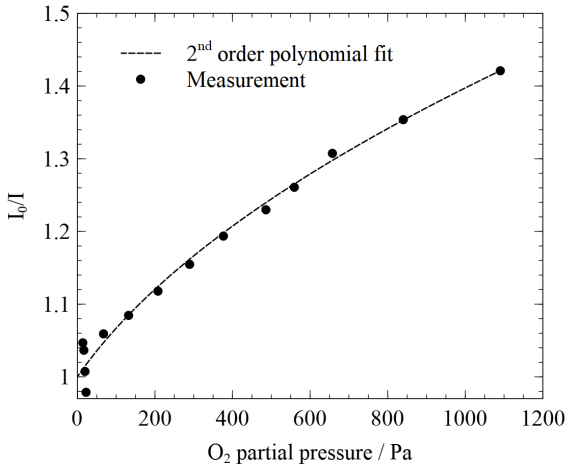


Fig 10. Average calibration data of the PSP measurements.

The illuminated paint absorbs the UV radiation and enters a higher internal energy state. Relaxation from this energy state occurs through the emission of photons in the red wavelength spectrum, i. e. through fluorescence. However, the presence of oxygen quenches the excited state and thus inhibits the fluorescence that would naturally occur [48, 49]. Thus, the paint emission intensity is sensitive to the partial pressure of molecular oxygen at the surface. The emitted red light is redirected by a flat mirror that is also mounted within the test section. The reflected light exits through the side windows of the test section and eventually reaches a high speed camera (Photron Mini-AX200 900K). A red long pass filter is attached in front of the camera lens to isolate the fluorescence signal of the PSP. The acquired images feature a bit depth of 12 with a 1024 $\times$ 848 pixel resolution, a frame rate of 8100 Hz and a shutter speed of 62 μs. The acquisition begins before flow arrival and captures the entire experiment.

Before an experiment, the PSP is calibrated in-situ by varying the test chamber pressure and recording the emitted radiation under different static conditions. The pressure is monitored using a high accuracy Inficon CDG025D pressure sensor which has an uncertainty of 266 Pa (accuracy as stated by manufacturer). The average measured intensity $I(p_{O2})$ at different oxygen partial pressures p_{O2} is shown in Fig. 10. The scatter of measurement points near absolute vacuum is most likely due to a difference in the LED excitation energy between tests and due to the degradation of the paint. The scatter can be used as a first estimate of the uncertainty of the calibration. For each pixel, the measured dependence is used to extrapolate to the expected intensity at absolute vacuum, i. e. a Stern-Volmer extrapolation. This reference intensity, denoted $I_{\text{ref}}(i,j)$ of pixel i, j, is then used to normalise each pixel intensity recorded during the calibration. A second order polynomial of the form

$$p_{O2}(i,j) = A_2(i,j)\left(\frac{I_{\text{ref}}(i,j)}{I(i,j)}\right)^2 + A_1(i,j)\frac{I_{\text{ref}}(i,j)}{I(i,j)} + A_0(i,j) \tag{3}$$

is then fitted to the normalised data. An example of that fit is shown for the average data in Fig. 10.

Since the PSP covered area, the mirror in the test section and the camera are not in the same optical plain, the recorded image is skewed and distorted. To retreive the original rectangular shape of the PSP area, an image reconstruction is performed. The spatial distribution of the recorded data is warped by a projective transformation to represent the original shape. Furthermore, a two-dimensional median filter with a length of 5 $\times$ 5 pixels is applied to the measurement. The resulting spatial resolution of the linear part of Eq.(3) is shown in Fig. 11. The data shows a very uniform even behaviour except for the sensor locations where no paint is present. During the presence of the flow, the mirror mounted in the test section suffers from slight vibrations. This results in a minor shaking of the recorded PSP area. An

Copyright © 2018 by the author(s)

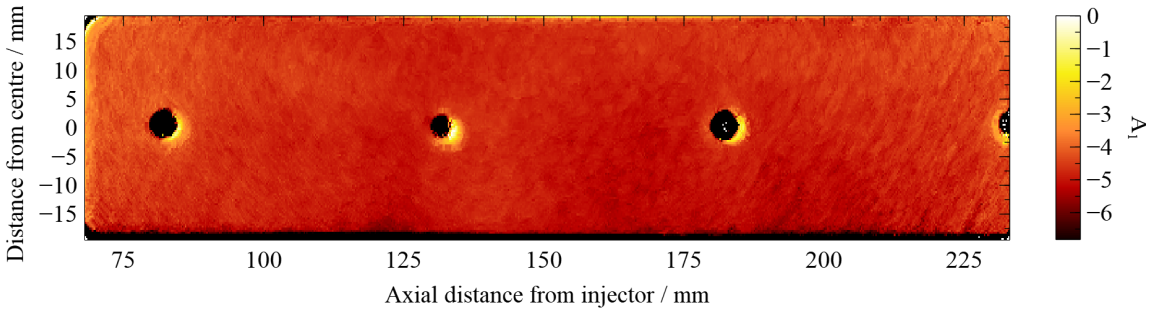


Fig 11. Spatial resolution of the coefficient A_1 in Eq. (3).

image stabilisation algorithm is used to correct for this movement [50].

The measured intensity over the time of the experiment is normalised by the intensity just prior to the start of the experiment $I_{\text{initial}}(i,j)$ when the conditions in the test section are very close to vacuum. To correct for the deviation from vacuum, the oxygen partial pressure calibration data is rescaled to the reference intensity $I_{\text{initial}}(i,j)$ and the calculation

$$p_{O2}(i,j) = A_2(i,j)\left(\frac{I_{\text{initial}}(i,j)}{I(i,j)}\right)^2 + A_1(i,j)\frac{I_{\text{initial}}(i,j)}{I(i,j)} + A_0(i,j) - p_{O2,\,\text{initial}} \tag{4}$$

is carried out for each pixel.

To evaluate film effectiveness, two separate tests have to be performed. First, air is injected at the desired blowing ratio. This then establishes the overall pressure footprint $p_{O2,\,\text{air}}$ with mass injection. In a second experiment, the same flow conditions are used and the foreign gas, e. g. N_2 or CO_2, is injected. The coolant film will prevent oxygen from reaching the surface which results in a different measured oxygen partial pressure $p_{O2,\,\text{foreign}}$. The two pressure traces and the respective molecular weights of air W_{air} and the foreign gas W_{foreign} are used to calculate the film effectiveness by evaluating[51]

$$\eta = 1 - \left[\left(\frac{p_{O2,\,\text{air}}}{p_{O2,\,\text{foreign}}} - 1\right)\frac{W_{\text{foreign}}}{W_{\text{air}}} + 1\right]^{-1}. \tag{5}$$

3. Results

This section presents the measurement results obtained during the experimental campaign. In the following two subsections, the data gathered with conditions 1 to 3 is reduced and the effect of free stream Reynolds number at the injection location and blowing ratio is studied. The emphasis of the analysis is on the mixing behaviour of the downstream film after the injection location. In the current analysis, only the results with Air and N_2 injection are considered.

3.1. Slot injector

This section provides an analysis of the measurement with the slot injector piece at flow condition 1. Figures 12 to 16 show Schlieren photographs during the second plateau at a Reynolds number of $\text{Re}_{\text{injector}} = 2.24 \cdot 10^6$ with various blowing ratios of air injection. A detail view of the respective boundary layers is provided in Fig. 17. The comparably strong shock in the upper part of Fig 16 stems from the boundary layer onset at the leading edge which poses a obstacle for the flow. The resulting redirection of the streamlines around the boundary layer leads to the visible shock above the flat plate. Even at no injection the slots induce a weak shock that is visible at approximately 5 mm from the injector location. A second shock is visible at approximately 20 mm downstream which could either be due to an irregularity in the model surface or be a product of the subsequent transition to turbulence. The incoming boundary layer, the white line above the surface, appears to be laminar as the Schlieren image shows an even

Copyright © 2018 by the author(s)

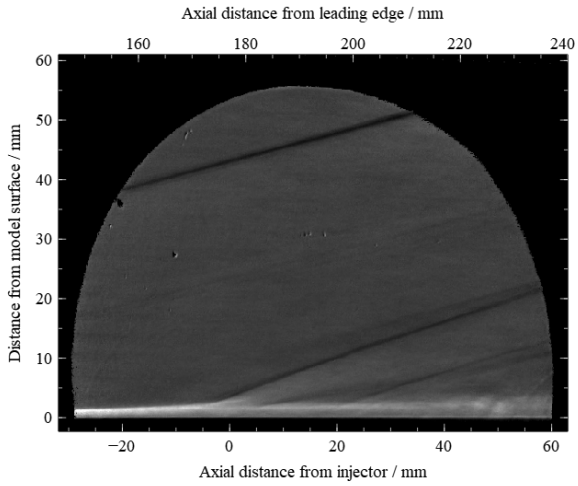


Fig 12. Schlieren Image at $\mathrm{Re}_{\mathrm{injector}} = 2.24 \cdot 10^6$ and air injection of $F = 0.20$ (condition 1).

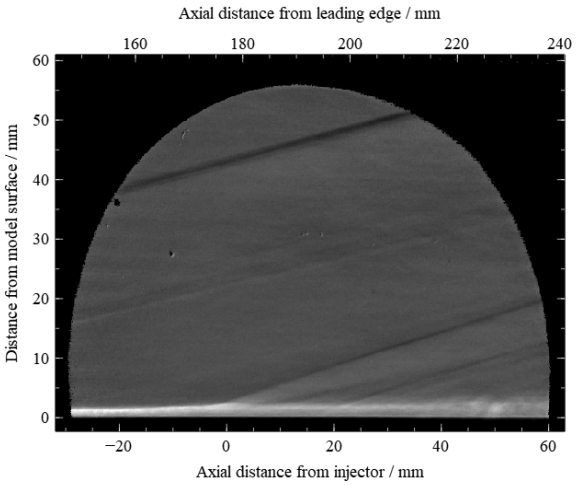


Fig 13. Schlieren Image at $\mathrm{Re}_{\mathrm{injector}} = 2.24 \cdot 10^6$ and air injection of $F = 0.11$ (condition 1).

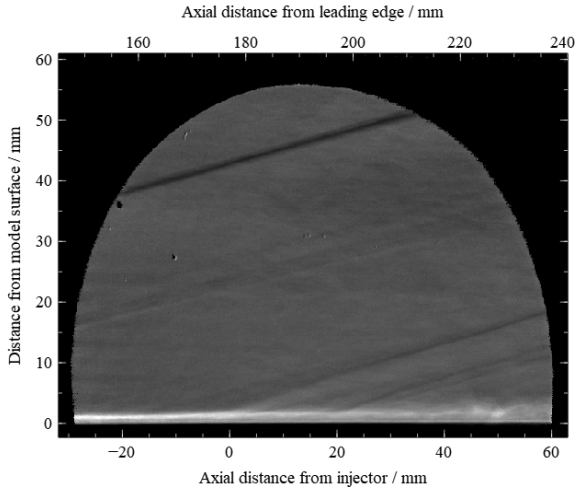


Fig 14. Schlieren Image at $\mathrm{Re}_{\mathrm{injector}} = 2.24 \cdot 10^6$ and air injection of $F = 0.075$ (condition 1).

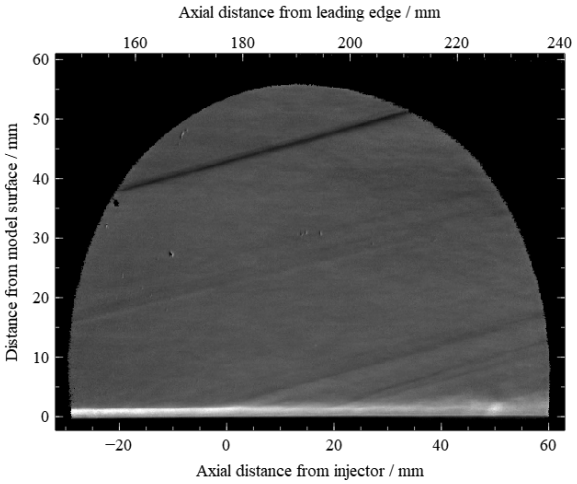


Fig 15. Schlieren Image at $\mathrm{Re}_{\mathrm{injector}} = 2.24 \cdot 10^6$ and air injection of $F = 0.058$ (condition 1).

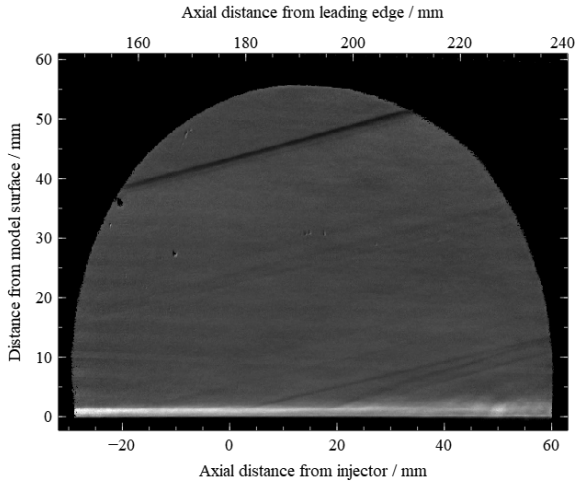


Fig 16. Schlieren Image at $\mathrm{Re}_{\mathrm{injector}} = 2.24 \cdot 10^6$ and air injection of $F = 0$ (condition 1).

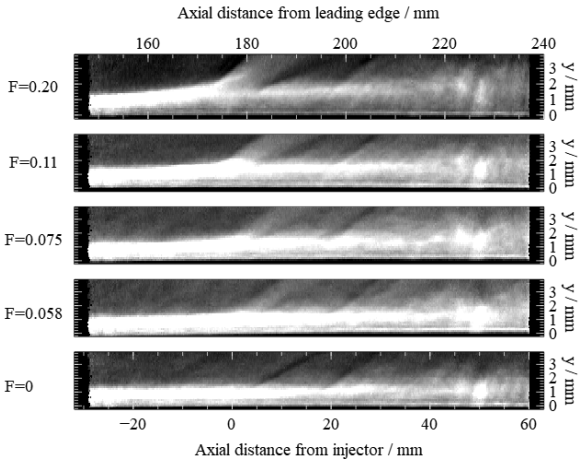


Fig 17. Boundary layer of Figs. 12 to 16.

Copyright © 2018 by the author(s)

density gradient. Between 20 mm and 40 mm the flow begins to transition to turbulence which is clearly visible due to the fragmented boundary layer shape and the general thickening of it.

The injection of coolant gas leads to various alterations of the flowfield. With an increase of injected gas, i. e. a higher blowing ratio, the boundary layer is thickened more and more. The thickened boundary layer again leads to a compression of the flow which is visible in the Schlieren image as a weak shock. As expected, a higher blowing ratio leads to a stronger shock. The boundary layer thickening even extends to an upstream location which is possible by the propagation of pressure information through the subsonic region of the boundary layer. This effect is apparent due to the injection shock which moves further upstream when the blowing ratio is increased. Furthermore, the injection also moves the transition location further upstream. A more fragmented boundary layer shape is observed when the blowing ratio is increased, which means that the boundary layer is tripped by the injection through the slots.

Figures 18 to 20 present the heat flux measurements at their respective locations downstream of the injection for various Reynolds numbers and blowing ratios. The error bars indicate the standard deviation of the measured heat flux during the steady state plateaus. As inferred from the Schlieren photography, the boundary layer state at the heat transfer gauge locations is turbulent (for $\mathrm{Re}_{\mathrm{injector}} = 2.24 \cdot 10^6$). Even with a turbulent heat transfer coefficient, the relatively low total temperature of the flow leads to a comparably small heat flux. Without injection, the heat flux increases for an increasing Reynolds number, as would be expected for turbulent boundary layer heat transfer on a flat plate. For the three largest Reynolds numbers, a low blowing ratio leads to a slight increase of heat transfer. Most likely, the injection leads to early transition and the added coolant gas does not contribute enough cool gas to counteract this increase in heat transfer. If the blowing ratio is further increased, the mass addition outweighs the early transition and a decrease in heat transfer is observed. In the case of the lowest Reynolds number $\mathrm{Re}_{\mathrm{injector}} = 1.36 \cdot 10^6$, the mass addition leads shows a significantly weaker influence on the change in heat transfer. In this case, the boundary layer is more likely to remain laminar for a longer distance along the plate's spanwise direction. Hence, an early transition is more detrimental. Heat flux increase and cooling through injection seem to balance each other.

Figures 21 and 22 show the effect on the surface pressure through the injection of coolant gas. For all studied Reynolds numbers, a higher blowing ratio leads to a very slight decrease in surface pressure downstream of the injection. The reason for this effect could possibly stem from flow spillage which is induced through the injection of additional gas through the slots. This tree-dimensional flow effect will be investigated in a future analysis including a comparison to numerical simulations of the experiment.

Figures 23 to 26 present the average axial film effectiveness for various Reynolds numbers and blowing ratios. The spatially resolved measurements are presented in Figs. 27 and 28. As expected, a higher blowing ratio tends to result in a higher film effectiveness close to the injection location as more added coolant mass produces a thicker film that keeps the free stream oxygen away from the model surface. This trend is true for all Reynolds numbers. At the highest Reynolds number $\mathrm{Re}_{\mathrm{injector}} = 2.40 \cdot 10^6$, blowing ratios below 0.093 seem to result in almost no film coverage. This is most likely due to the very efficient turbulent mixing of external flow and coolant gas. When the Reynolds number is slightly lower ($\mathrm{Re}_{\mathrm{injector}} = 2.24 \cdot 10^6$), even those small blowing ratios result in a much better film effectiveness. Furthermore, it is observed that a higher blowing ratio leads to a higher film effectiveness close to the injection location. However, especially in the case of the lowest Reynolds number ($\mathrm{Re}_{\mathrm{injector}} = 1.36 \cdot 10^6$, Fig. 23), the largest blowing ratio ($F = 0.32$) results in an earlier diminishing of the film effectiveness for locations further downstream. It is gathered from Fig. 27 that this effect is mainly caused by an increased lateral mixing of the coolant gas with the surrounding flow. This effect leads to the characteristic "V"-shape of the film effectiveness. A decrease in blowing ratio ($F = 0.18$) shows a dramatic improvement of the film effectiveness further downstream. There is decreased lateral mixing, thus, the film covers a much greater area. A general trend that can be extracted from Figs. 27 and 28 is that a blowing ratio below 0.20 shows a much better film coverage of the downstream surface. Higher injection rates lead to a more and more prominent three-dimensional flow behaviour that results in the characteristic

Copyright © 2018 by the author(s)

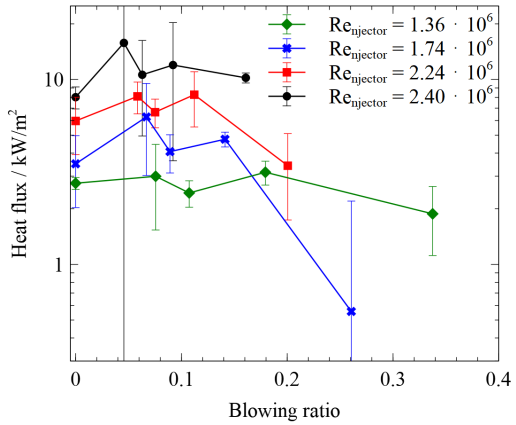


Fig 18. Heat flux at $x = 242$ mm (61 mm from slot injector) for different Reynolds numbers (condition 1).

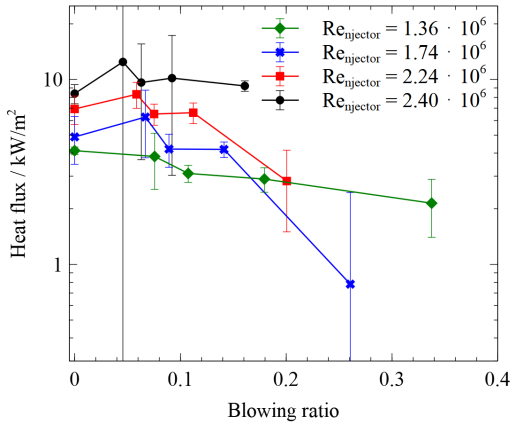


Fig 19. Heat flux at $x = 342$ mm (161 mm from slot injector) for different Reynolds numbers (condition 1).

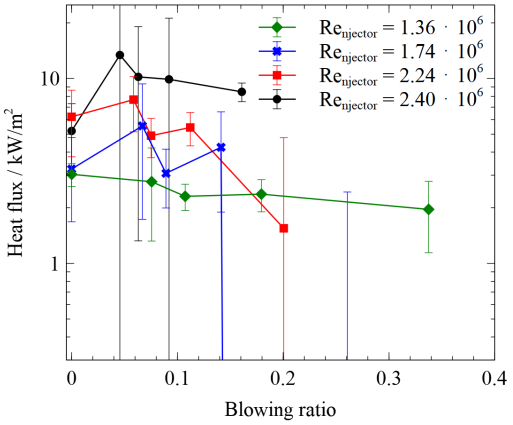


Fig 20. Heat flux at $x = 442$ mm (261 mm from slot injector) for different Reynolds numbers (condition 1).

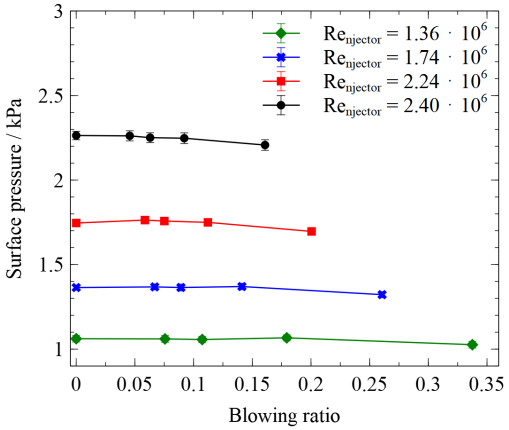


Fig 21. Surface pressure at $x = 292$ mm (111 mm from slot injector) for different Reynolds numbers (condition 1).

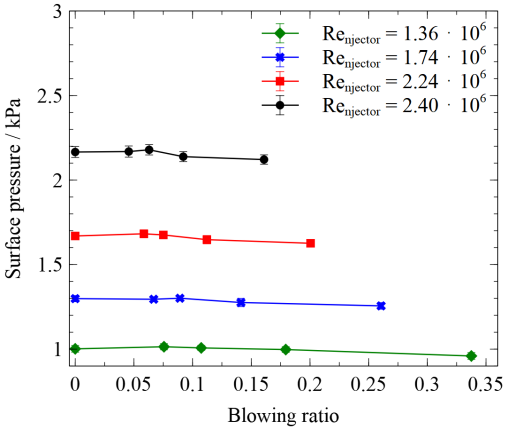


Fig 22. Heat flux at $x = 392$ mm (211 mm from slot injector) for different Reynolds numbers (condition 1).

Copyright © 2018 by the author(s)

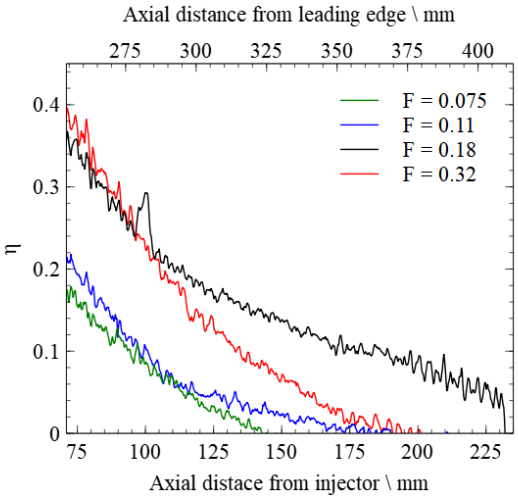


Fig 23. Axial mean of the film effectiveness for $Re_{injector} = 1.36 \cdot 10^6$ (condition 1).

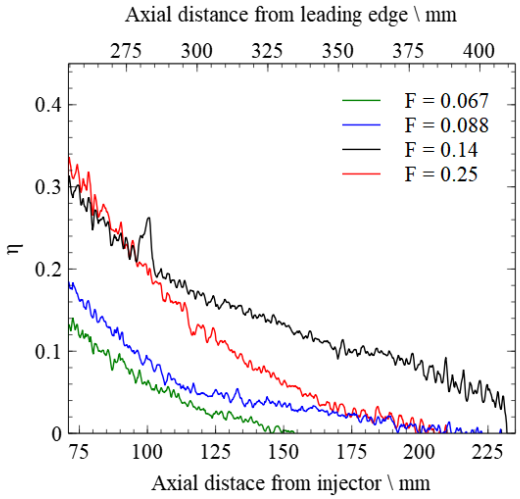


Fig 24. Axial mean of the film effectiveness for $Re_{injector} = 1.74 \cdot 10^6$ (condition 1).

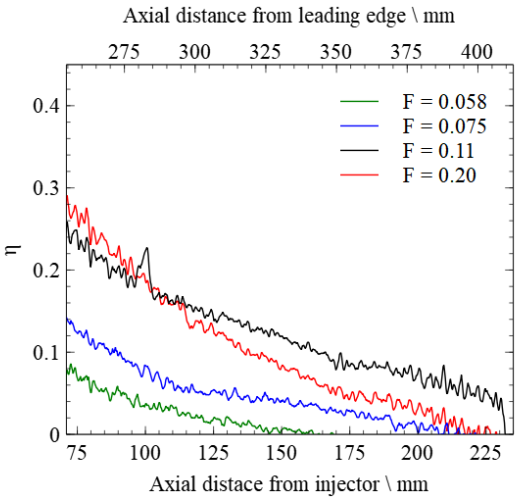


Fig 25. Axial mean of the film effectiveness for $Re_{injector} = 2.24 \cdot 10^6$ (condition 1).

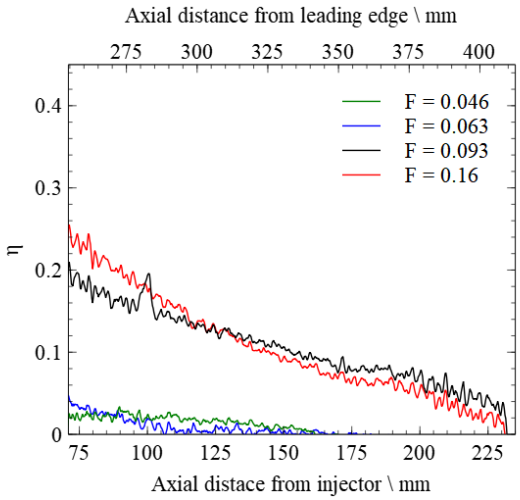


Fig 26. Axial mean of the film effectiveness for $Re_{injector} = 2.40 \cdot 10^6$ (condition 1).

Copyright © 2018 by the author(s)

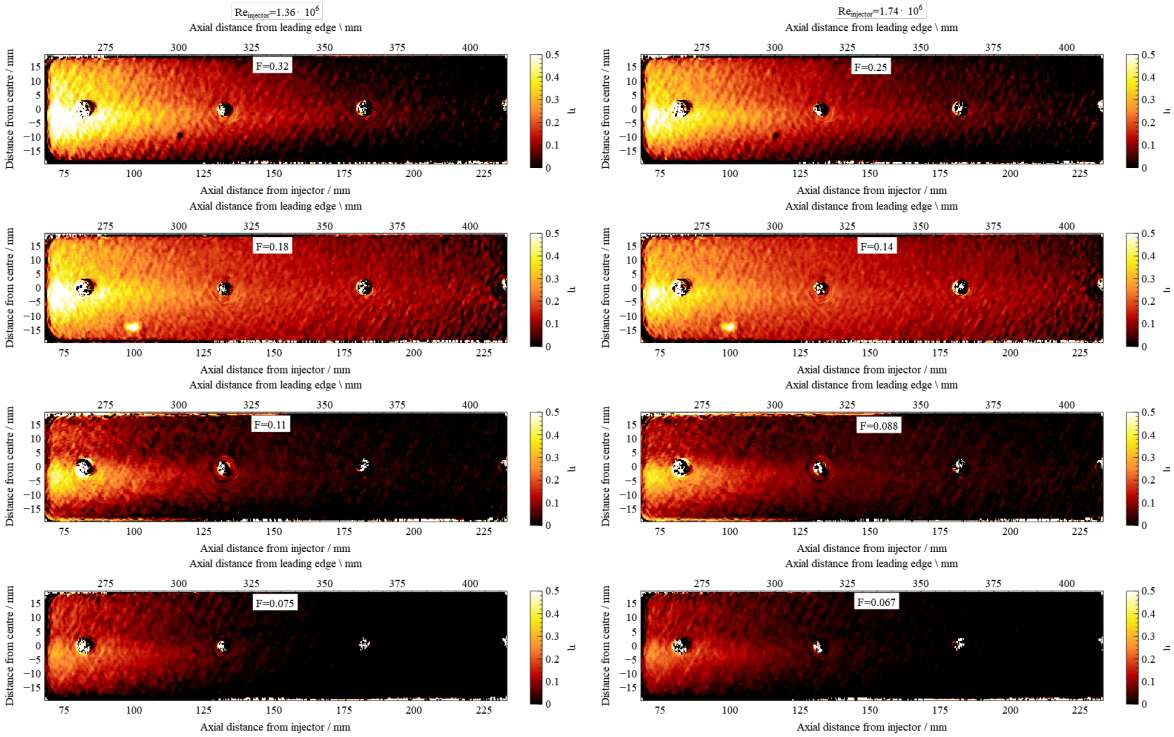


Fig 27. Film effectiveness with the slot injector piece for $\mathrm{Re}_{\mathrm{injector}} = 1.36 \cdot 10^6$ and $\mathrm{Re}_{\mathrm{injector}} = 1.74 \cdot 10^6$.

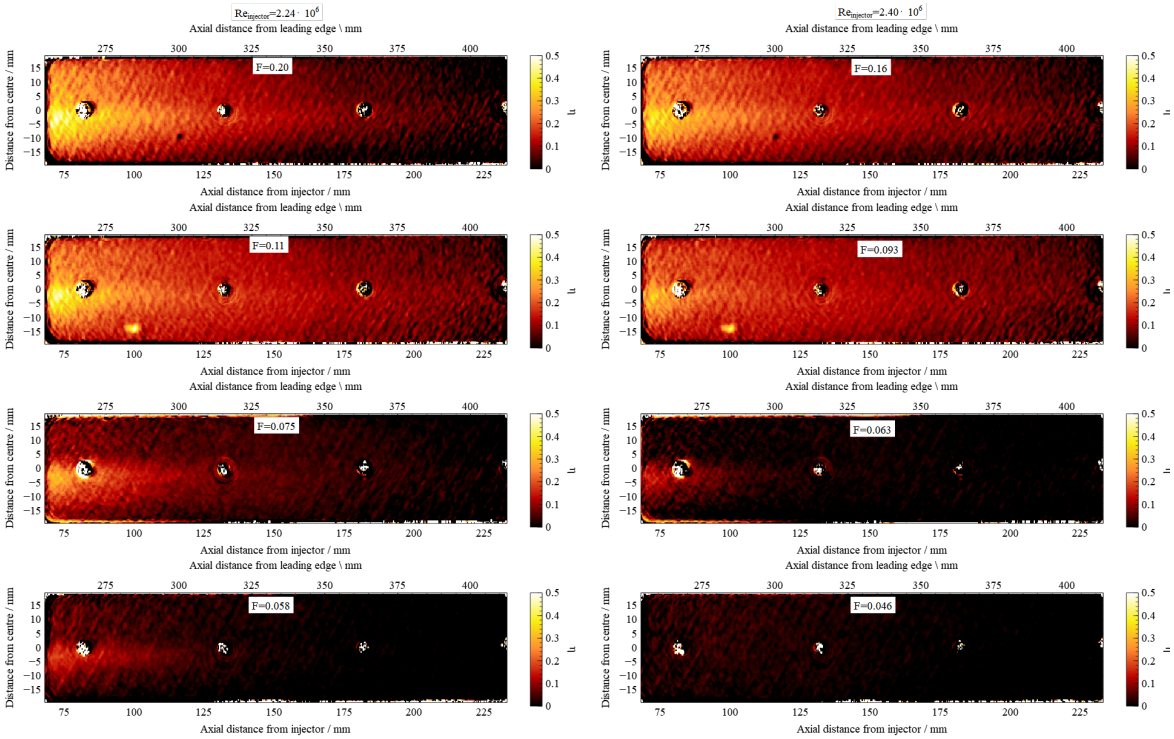


Fig 28. Film effectiveness with the slot injector piece for $\mathrm{Re}_{\mathrm{injector}} = 2.24 \cdot 10^6$ and $\mathrm{Re}_{\mathrm{injector}} = 2.40 \cdot 10^6$.

Copyright © 2018 by the author(s)

"V"-shape and hence worse film coverage.

Another trend observed from the measurements is the effect of free stream Reynolds number on the diminishing of the film. For example, a blowing ratio of $F = 0.11$ at a Reynolds number of $\mathrm{Re}_{\mathrm{injector}} = 1.36 \cdot 10^6$ exhibits a much steeper η-profile as the same blowing ratio for $\mathrm{Re}_{\mathrm{injector}} = 2.24 \cdot 10^6$. The spatial distribution of the film effectiveness again shows that the difference is mainly due to the higher lateral flow mixing in the case of the lower Reynolds number. This observation is counter-intuitive as a higher Reynolds number should lead to more efficient mixing. Possibly, a lower Reynolds number flow experiences a more impactful influence of mass injection.

3.2. Porous injector (UHTC)

This section details the results obtained with the porous injector piece at flow conditions 2 and 3. Figures 29 to 33 present the Schlieren photographs during the second plateau of condition 2 at various blowing ratios. A detailed view of the respective boundary layers is shown in Fig. 34. The baseline case of no injection for a Reynolds number of $\mathrm{Re}_{\mathrm{injector}} = 2.04 \cdot 10^6$ is presented in Fig. 31. The boundary layer is laminar and undergoes a natural transition to turbulence downstream of the porous sample. Two very weak shocks are induced at the beginning and the end of the injector. The two shocks in the centre of the image stem from the sides of the model and do not influence the centre of the plate. The injection through the porous sample leads to a gradual thickening of the boundary layer along the injector piece. The injection with $F = 0.0020$ appears to have no significant effect on the transition location. However, the injection at $F = 0.0064$ leads to a much thicker boundary layer and a transition that starts on the sample itself. In comparison to the slot injector, the induced shock due to the mass addition into the boundary layer is much weaker. This is no surprise as the injected mass flux is two orders of magnitude lower and the injection occurs over a much longer area which leads to a more gradual increase of boundary layer thickness and hence a less immediate compression of the boundary layer edge streamline. Although the blowing ratio is much lower than for the slot injection, the boundary layer thickness is larger, e. g. The difference between Figs. 12 and 29. This indicates that the coolant gas tends to stay much closer to the model surface when it is injected through the porous wall and hence inhibits mixing of the surrounding flow and the coolant layer.

An alternative case is presented in Figs. 32 and 33 which show the Schlieren photographs for the case of flow condition 3. The baseline case of no injection shows that the boundary layer stays laminar throughout the entire observed flowfield. The coolant injection at $F = 0.011$ leads to transition to turbulence on the porous sample. Furthermore, a gradual compression area is observed in front of the sample.

The downstream heat flux dependence on blowing ratio for various Reynolds numbers is presented in Figs. 35 to 37. For intermediate Reynolds numbers, $2.18 \cdot 10^6 < \mathrm{Re}_{\mathrm{injector}} < 1.24 \cdot 10^6$, A low injection ratio leads to a dramatic cooling effect. This observation coincides with the Schlieren photography where a significant thickening has been observed, but no earlier transition. If the blowing ratio is further increased the earlier onset of transition diminishes the cooling effect and the measured heat flux increases, as is in accordance with the observations of the Schlieren photographs. In the case of the most downstream thin film gauge, the measured heat flux is even slightly below zero and hence not displayed in the logarithmic plot. Therefore, it can be concluded that a critical blowing ratio exists for a specific Reynolds number regime that causes an early transition. The case of $\mathrm{Re}_{\mathrm{injector}} = 1.24 \cdot 10^6$ shows the same characteristics but at a later location, i. e. $x = 442$ mm. For the highest Reynolds number $\mathrm{Re}_{\mathrm{injector}} = 2.18 \cdot 10^6$, the same trend is observed but much less pronounced. As the high Reynolds number flow tends to increase mixing due to an earlier onset of turbulence, the cooling is less effective. In the case of the lowest Reynolds number $\mathrm{Re}_{\mathrm{injector}} = 0.55 \cdot 10^6$, a strong cooling effect is noticed at $x = 242$ mm but almost no effect on the heat flux is apparent for locations further downstream. Close to the injection point, the cooling leads to an effective film coverage which is lost further downstream due to the flow mixing.

Figures 38 and 39 present the downstream surface pressure at different Reynolds numbers and blowing ratios. Analogously to the case of injection through slots, a slight decrease of surface pressure is

Copyright © 2018 by the author(s)

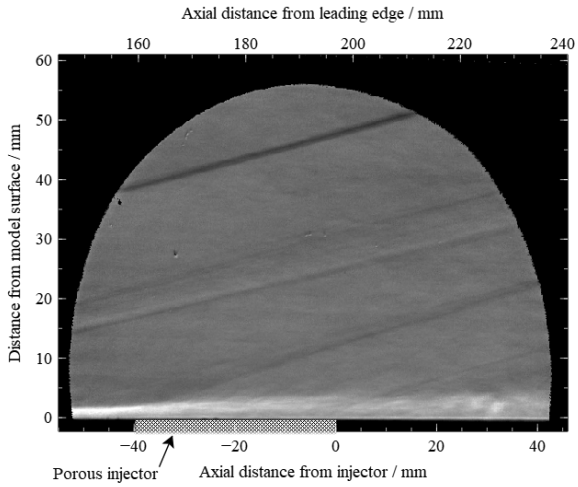


Fig 29. Schlieren Image at $\mathrm{Re}_{\mathrm{injector}} = 2.04 \cdot 10^6$ and air injection of $F = 0.0064$ (condition 2).

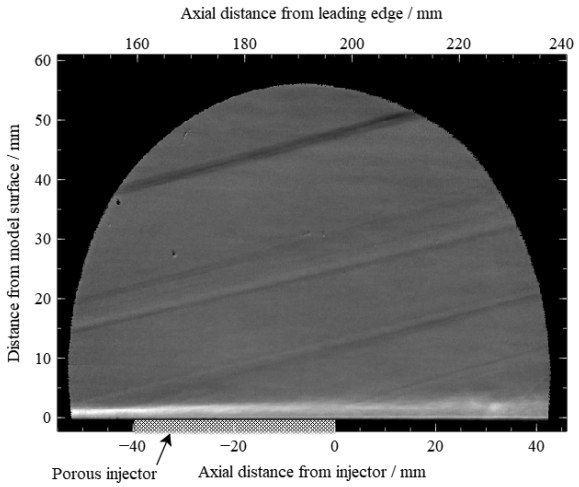


Fig 30. Schlieren Image at $\mathrm{Re}_{\mathrm{injector}} = 2.04 \cdot 10^6$ and air injection of $F = 0.0020$ (condition 2).

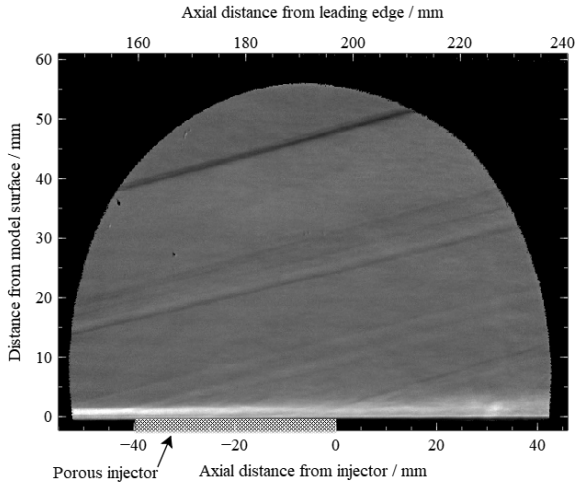


Fig 31. Schlieren Image at $\mathrm{Re}_{\mathrm{injector}} = 2.04 \cdot 10^6$ and air injection of $F = 0$ (condition 2).

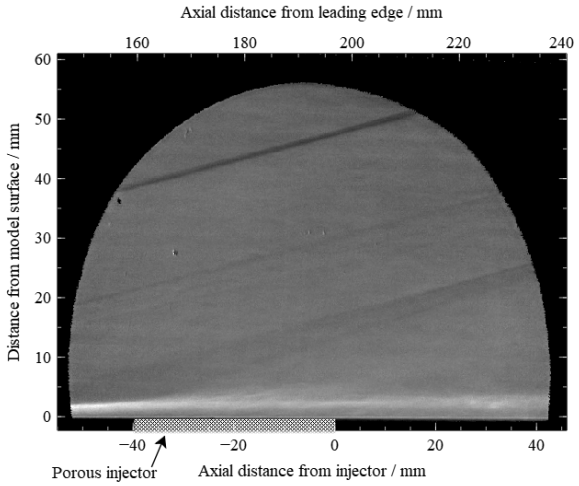


Fig 32. Schlieren Image at $\mathrm{Re}_{\mathrm{injector}} = 1.15 \cdot 10^6$ and air injection of $F = 0.011$ (condition 3).

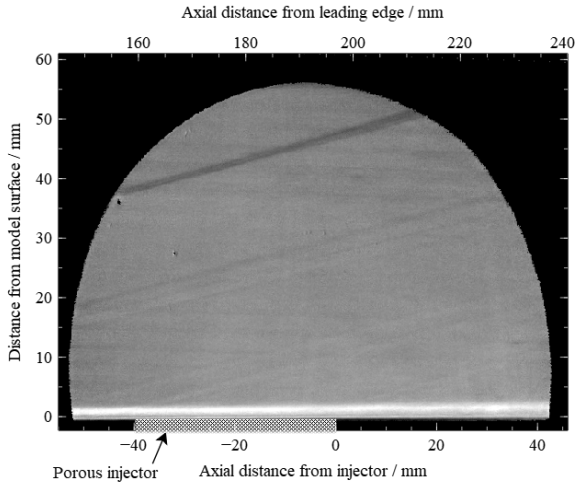


Fig 33. Schlieren Image at $\mathrm{Re}_{\mathrm{injector}} = 1.15 \cdot 10^6$ and air injection of $F = 0$ (condition 3).

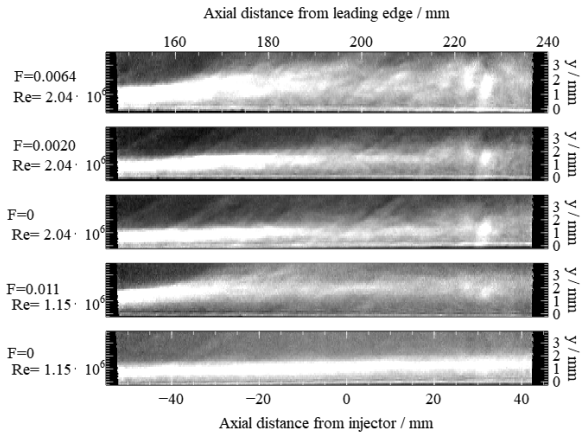


Fig 34. Boundary layer of Figs. 29 to 33.

Copyright © 2018 by the author(s)

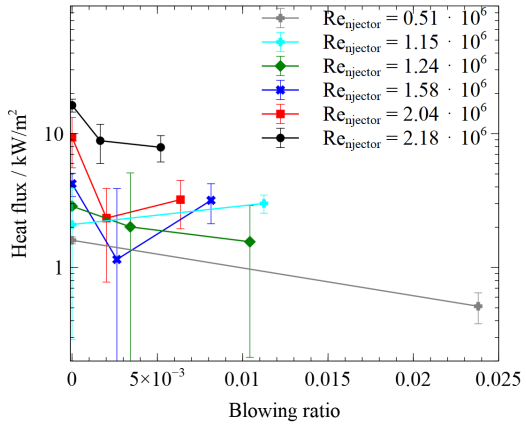


Fig 35. Heat flux at $x = 242$ mm (43 mm from porous injector) for different Reynolds numbers (conditions 2, 3).

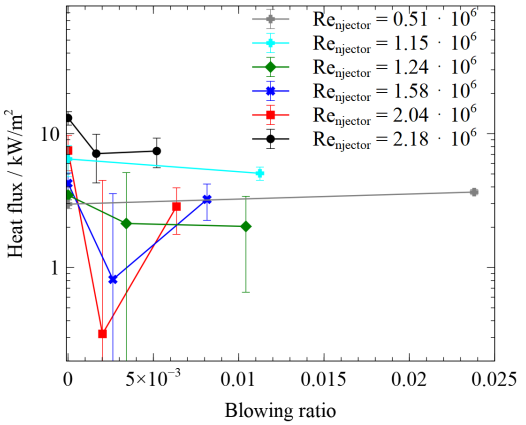


Fig 36. Heat flux at $x = 342$ mm (143 mm from porous injector) for different Reynolds numbers (conditions 2, 3).

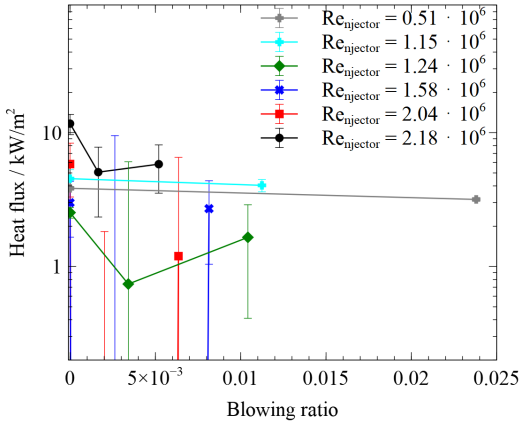


Fig 37. Heat flux at $x = 442$ mm (243 mm from porous injector) for different Reynolds numbers (conditions 2, 3).

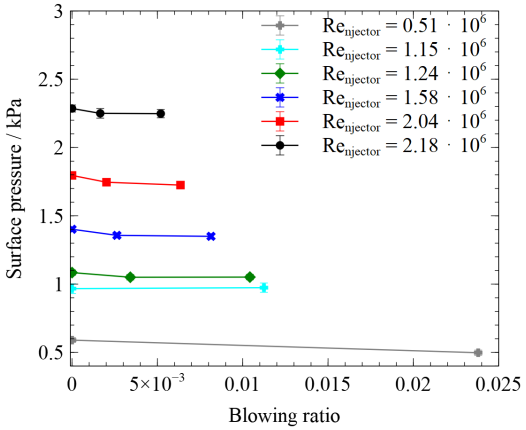


Fig 38. Surface pressure at $x = 292$ mm (93 mm from porous injector) for different Reynolds numbers (conditions 2, 3).

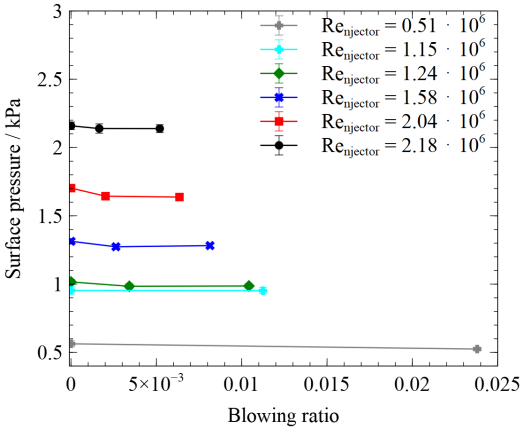


Fig 39. Heat flux at $x = 392$ mm (193 mm from porous injector) for different Reynolds numbers (conditions 2, 3).

Copyright © 2018 by the author(s)

observed when blowing occurs.

Figures 40 to 45 show the average film effectiveness downstream of thee porous sample at different Reynolds numbers. The spatial distribution is shown in Figs. 46 to 48. The most apparent outcome in comparison to the injection through slots is the vastly superior cooling performance. At the same flow conditions, similar levels of film effectiveness are achieved, but with two orders of magnitude lower blowing ratios. The homogeneous mass injection leads to a significantly lower amount of flow mixing which allows the coolant layer to remain more intact. At laminar flow conditions, e. g. at $\mathrm{Re}_{\mathrm{injector}} = 0.51 \cdot 10^6$, a maximum film effectiveness of 77 % is achieved for a blowing ratio of $F = 0.025$. However, the downstream effectiveness is poor. The mixing mechanism is identical to the slot injection, which means that mostly lateral flow mixing is responsible for the diminishing film effectiveness. The spatial distribution in Fig. 46 shows the characteristic "V"-shape which is more pronounced for higher blowing ratios. Hence, a very clear effect of the influence of a high blowing ratio on the mixing characteristics is found for laminar conditions.

The best downstream film performance for this boundary layer type is found for $F = 0.011$ at $\mathrm{Re}_{\mathrm{injector}} = 1.15 \cdot 10^6$. Although the Schlieren photograph has confirmed a transition to turbulence, the mixing of coolant gas and the external flow is delayed. Especially the mixing characteristics further downstream seem much less influenced by the lateral mixing and a stable broad film is established. For high Reynolds number conditions, similar characteristics as with the slot injector are obtained: A high blowing ratio leads to more lateral mixing and a faster breakdown of the film. As expected, an increase in blowing ratio leads to a better film effectiveness. This effect is most prominent for low blowing ratios, e. g. at $0.0016 < F < 0.0053$. For higher blowing ratios, e. g. for $0.0032 < F < 0.010$, more mass injection leads only to a slight increase in film effectiveness. A possible explanation could be the increasing disturbance of the boundary layer for higher injection rates which causes more mixing and hence a lower film coverage. The additional coolant mass is thus balanced with the increased flow mixing. The spatial distribution of the low blowing ratio cases, i. e. Fig. 48, shows that the mixing mechanism is different from the high injection ratios. The film shape is much more uniform and less "V"-shaped which means that lateral mixing is inhibited and vertical mixing is the dominant mechanism.

Copyright © 2018 by the author(s)

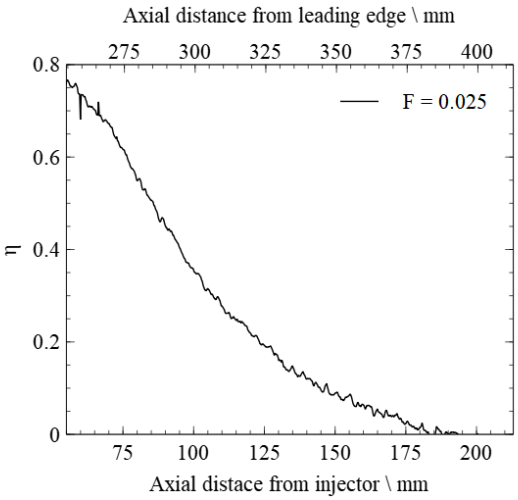


Fig 40. Axial mean of the film effectiveness for $Re_{injector} = 0.51 \cdot 10^6$ (condition 3).

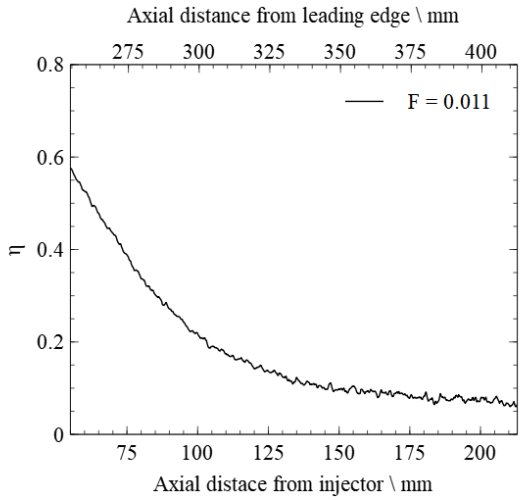


Fig 41. Axial mean of the film effectiveness for $Re_{injector} = 1.15 \cdot 10^6$ (condition 3).

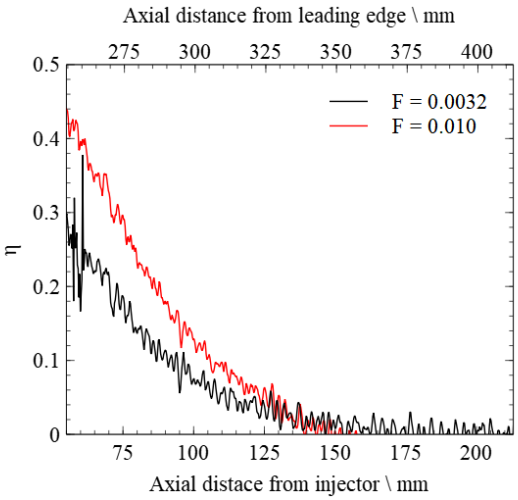


Fig 42. Axial mean of the film effectiveness for $Re_{injector} = 1.24 \cdot 10^6$ (condition 2).

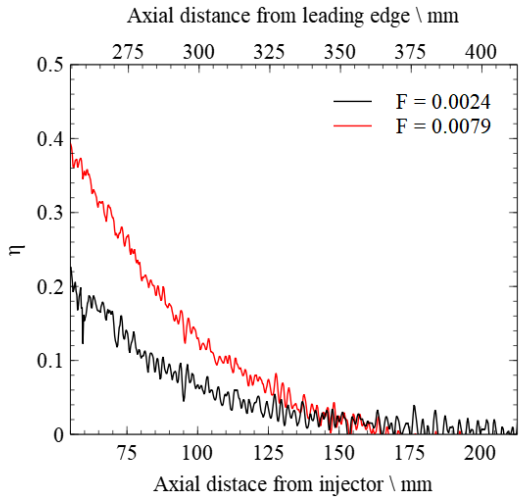


Fig 43. Axial mean of the film effectiveness for $Re_{injector} = 1.58 \cdot 10^6$ (condition 2).

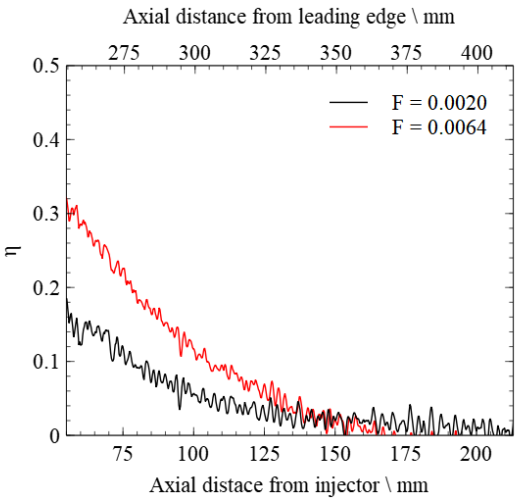


Fig 44. Axial mean of the film effectiveness for $Re_{injector} = 2.04 \cdot 10^6$ (condition 2).

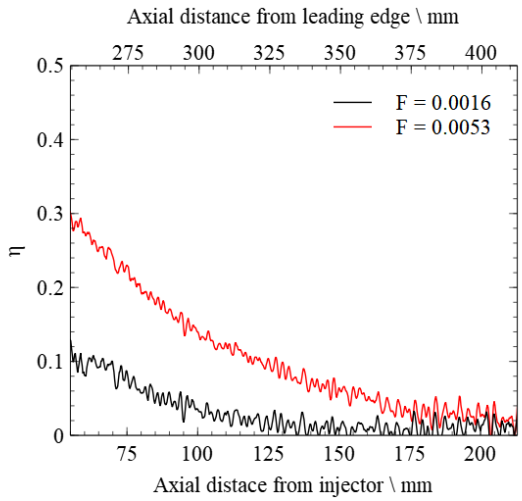


Fig 45. Axial mean of the film effectiveness for $Re_{injector} = 2.18 \cdot 10^6$ (condition 2).

Copyright © 2018 by the author(s)

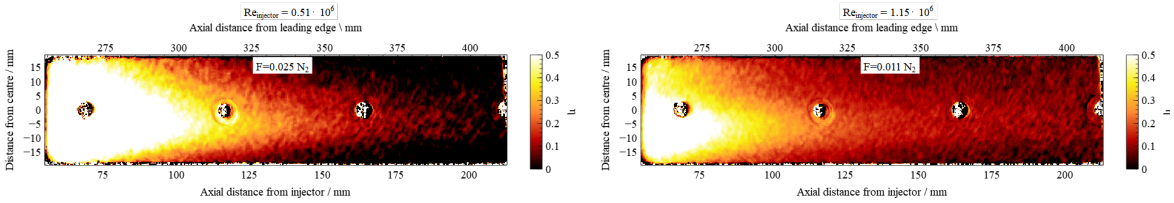


Fig 46. Film effectiveness with the porous injector piece for $\mathrm{Re}_{\mathrm{injector}} = 0.51 \cdot 10^6$ and $\mathrm{Re}_{\mathrm{injector}} = 1.15 \cdot 10^6$

.

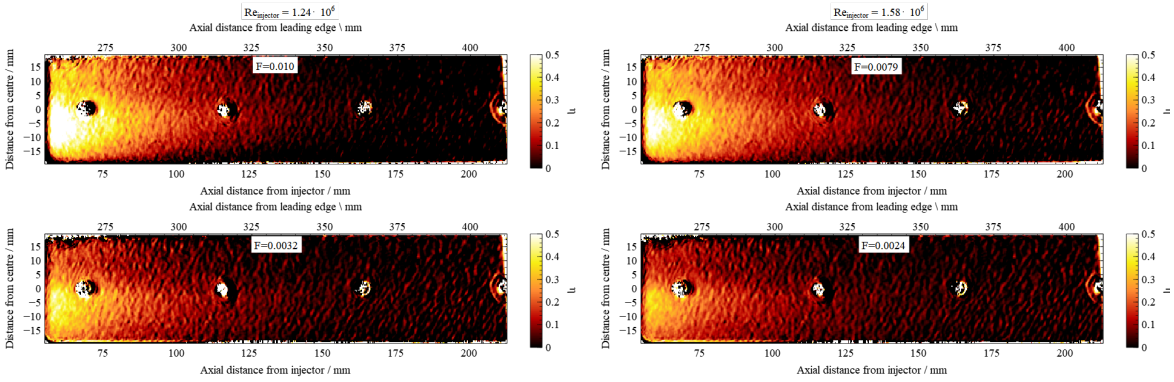


Fig 47. Film effectiveness with the porous injector piece for $\mathrm{Re}_{\mathrm{injector}} = 1.24 \cdot 10^6$ and $\mathrm{Re}_{\mathrm{injector}} = 1.58 \cdot 10^6$

.

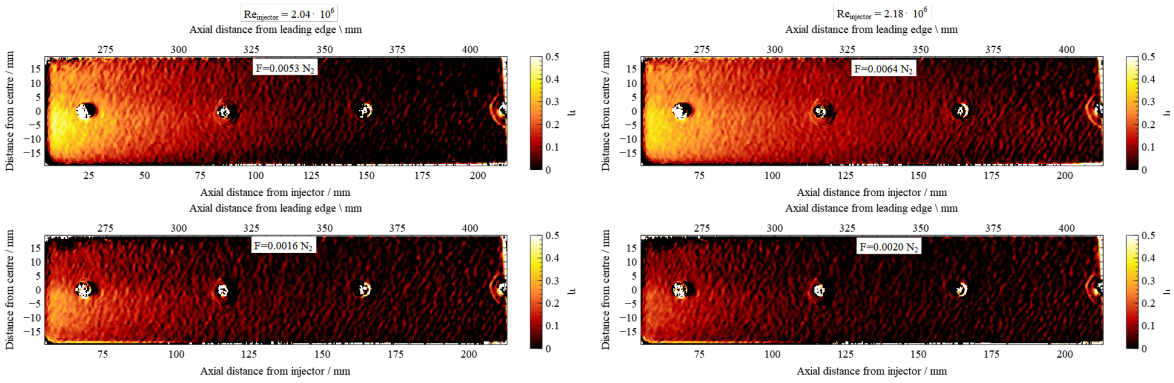


Fig 48. Film effectiveness with the porous injector piece for $\mathrm{Re}_{\mathrm{injector}} = 2.04 \cdot 10^6$ and $\mathrm{Re}_{\mathrm{injector}} = 2.18 \cdot 10^6$

.

Copyright © 2018 by the author(s)

4. Conclusion

This paper presents transpiration cooling experiments conducted in the Oxford High Density Tunnel. The flow structure and mixing phenomena between the injected coolant gas and the hypersonic free stream are investigated. A flat plate model is used which is equipped with a gas injection system, four surface mounted heat flux gauges and three surface pressure sensors located downstream of the injection point. Mass injection is realized through a porous ceramic material, and alternatively through a series of slots. Spatially and temporally resolved film effectiveness downstream of the injection point is measured with fast response pressure sensitive paint. The flowfield is visualised by a Z-type Schlieren imaging system.

Results show a significant influence of injection on the boundary layer thickness through the additional coolant gas. At low Reynolds numbers injection leads to early transition, even for very low blowing ratios. Although the heat flux close to the injection point is reduced significantly, locations further downstream do not profit as much from the coolant layer as it is fully mixed with the external flow. Transpiration cooling (porous injector) performs significantly better than effusion cooling (slot injector). Similar film effectiveness is achieved for two orders of magnitude lower mass injection. Generally, a higher blowing ratio leads to a higher film effectiveness. A significant effect of the blowing ratio with regards to the mixing mechanisms is identified. A low blowing ratio establishes a broad and stable film where the external flow mixes vertically with the coolant layer, i. e. a mostly two-dimensional flowfield behaviour prevails. For high blowing ratios, the lateral mixing from the sides of the coolant layer is the dominant effect. Here, three-dimensional flowfield effects become dominant.

The current study has identified a clear influence of various parameters on the flowfield for mostly turbulent or transitional flow conditions. In future experiments, laminar flow conditions and a wider range of blowing ratios will be investigated to add to the understanding of transpiration cooled flowfields.

Acknowledgments

The help and dedicated attention to detail of Greg King is greatly acknowledged. The authors would like to extend their gratitude towards the entire hypersonics group and the laboratory technical staff. The help in operating the facility by Christopher Hambidge is acknowledged. The authors additionally thank Laura Larrimbe, Daniel Glymond and Luc Vandeperre from Imperial College London for providing the material samples. Furthermore, the authors would like to thank Adriano Cerminara and Ralf Deiterding from the University of Southampton for their valuable input in the design phase of the slot injector.

References

[1] J. D. Anderson. *Hypersonic and High-Temperature Gas Dynamics, Second Edition*. AIAA Education Series, 2006.

[2] T. Hermann, I. Naved, and M. McGilvray. Performance of transpiration cooled heat shields for re-entry vehicles. In *AIAA Science and Technology Forum and Exposition*. San Diego, CA, January 2019. submitted.

[3] Hannah Boehrk, Olivier Piol, and Markus Kuhn. Heat balance of a transpiration-cooled heat shield. *Journal of Thermophysics and Heat Transfer*, 24(3):581–588, May 2010.

[4] M. Ewenz Rocher, T. Hermann, M. McGilvray, H. S. Ifti, F. Hufgard, Eberhart. M., A. Meindl, S. Loehle, and F. Zander. Testing a transpiration cooled zirconium-di-boride sample in the plasma tunnel at irs. In *22nd AIAA International Space Planes and Hypersonics Systems and Technologies Conference*, 2019.

[5] Christian Dittert, Markus Selzer, and Hannah Böhrk. Flowfield and pressure decay analysis of porous cones. *AIAA Journal*, 55(3):874–882, May 2018.

Copyright © 2018 by the author(s)

[6] Burkard Esser, Ali Gülhan, Thomas Reimer, and Ivaylo Petkov. Experimental verification of thermal management concepts for space vehicles. In *8th European Symposium on Aerothermodynamics for Space Vehicles*, number 91674 in Conference Proceedings online, pages 1–8, 2015.

[7] S. Mohammed Ibrahim, P. Vivek, and K. P. J. Reddy. Experimental investigation on transpiration cooling effectiveness for spacecraft entering martian atmosphere. *AIAA Journal*, 54(9):2922–2926, May 2018.

[8] H. Böhrk, H. Elsässer, and H. Weihs. Flight data from the faceted tps on shefex ii. In *8th European Symposium on Aerothermodynamics for Space Vehicles*, 2015.

[9] M. Kuhn and H. Hald. Application of transpiration cooling for hot structures. In Ali Gülhan, editor, *RESPACE - Key Technologies for Reusable Space Systems*, pages 82–103, Berlin, Heidelberg, 2008. Springer Berlin Heidelberg.

[10] Yuan-Qing Liu, Peixue Jiang, Shao-Shan Jin, and Ji-Guo Sun. Transpiration cooling of a nose cone by various foreign gases. *International Journal of Heat and Mass Transfer*, 53:5364–5372, November 2010.

[11] Kevin D. Basore, Marcus Selzer, Vincent Wheatley, Russell R. Boyce, David J. Mee, Bianca R. Capra, Markus Kuhn, and Stefan Brieschenk. Performance comparison of distributed injection methods for hypersonic film-cooling. In *20th Australasian Fluid Mechanics Conference*, Perth, WA, December 2016. Australasian Fluid Mechanics Society.

[12] Friedolin Strauss, Manuel Wößner, Matthias Weißwange, Chiara Manfletti, and Stefan Schlechtriem. Experiments on flow interaction in a transpiration cooled model scramjet. In *7th European Conference for Aeronautics and Space Science (EUCASS)*, Juli 2017.

[13] Tobias Langener, Jens Von Wolfersdorf, and Johan Steelant. Experimental investigations on transpiration cooling for scramjet applications using different coolants. *AIAA Journal*, 49(7):1409–1419, May 2011.

[14] A. Guelhan and S. Braun. An experimental study on the efficiency of transpiration cooling in laminar and turbulent hypersonic flows. *Experiments in Fluids*, 50(3):509–525, March 2011.

[15] H. Tanno, T. Komuro, K. Itoh, Markus Kuhn, Ivaylo Petkov, and B. Esser. Transpiration cooling experiments in free-piston shock tunnel hiest. In *8th European Workshop on Thermal Protection Systems and Hot Structures*, July 2016.

[16] Matthew McGilvray, Luke J. Doherty, Andrew J. Neely, Robert Pearce, and Peter Ireland. The oxford high density tunnel. In *20th AIAA International Space Planes and Hypersonic Systems and Technologies Conference*, number 0 in International Space Planes and Hypersonic Systems and Technologies Conferences. American Institute of Aeronautics and Astronautics, October 2015.

[17] Sebastien Wylie, Luke Doherty, and Matthew McGilvray. Commissioning of the oxford high density tunnel (hdt) for boundary layer instability measurements at mach 7. Number 0 in AIAA AVIATION Forum. American Institute of Aeronautics and Astronautics, October 2018.

[18] Hassan Saad Ifti, Tobias Hermann, and Matthew McGilvray. Flow characterisation of transpiring porous media for hypersonic vehicles. In *22nd AIAA International Space Planes and Hypersonics Systems and Technologies Conference*, Orlando, Florida, 2018.

[19] H. Tanno. Thor - innovative thermal management concepts for thermal protection of future space vehicles, validation test results from shock tunnel facility. Technical Report D6.5, JAXA, 2015.

[20] Markus Kuhn, Hermann Hald, Ali Gülhan, Burkard Esser, and Herbert Olivier. Experimental investigations of transpiration cooled cmc's in supersonic plasma flows. In *European Space Agency, (Special Publication) ESA SP*, volume 631, pages 1–8, July 2006.

Copyright © 2018 by the author(s)

[21] B. Esser. Thor - innovative thermal management concepts for thermal protection of future space vehicles, validation test results in arc-heated facilities part c: Active cooling concept 2b. Technical Report D6.3, DLR, 2015.

[22] Jianye Wang and L. Vandeperre. *Deformation and Hardness of UHTCs as a Function of Temperature*. October 2014.

[23] Tobias Hermann, Matthew McGilvrayy, and Hassan Saad Ifti. Fluid-solid heat exchange in porous media for transpiration cooling systems. In *AIAA Science and Technology Forum and Exposition*, San Diego, California, January 2019.

[24] Fabian Hufgard, Stefan Loehle, Jens von Wolfersdorf, Johan Steelant4, Tobias Hermann, and Matthew McGilvray. Analysis of porous materials for transpiration-cooled heat flux sensor development. In *International Conference on High-Speed Vehicle Science Technology*, Moscow, Russia, 2018.

[25] Fabian Hufgard, Stefan Loehle, Jens von Wolfersdorf, Stefanos Fasoulas, Marc Ewenz Rocher, Tobias Hermann, Matthew McGilvray, and Johan Steelant. Surface heat flux measurement in transpiration-cooled porous materials using plenum pressure data. In *AIAA Science and Technology Forum and Exposition*, San Diego, CA, 2019.

[26] M. Balat-Pichelin, E. Bêche, D. Sciti, and D. Alfano. Emissivity, catalycity and microstructural characterization of zrb2-sicfiber based uhtc at high temperature in a non-equilibrium air plasma flow. *Ceramics International*, 40(7, Part A):9731–9742, August 2014.

[27] M. W. Chase, National Institute of Standards, and Technology (U.S.). *NIST-JANAF thermochemical tables*. American Chemical Society ; American Institute of Physics for the National Institute of Standards and Technology, [Washington, D.C.]; Woodbury, N.Y., 1998.

[28] Adriano Cerminara, Ralf Deiterding, and Neil Sandham. Dns of hypersonic flow over porous surfaces with a hybrid method. Number 0 in AIAA SciTech Forum. American Institute of Aeronautics and Astronautics, October 2018.

[29] Jens Meinert, J-ograve, rg Huhn, Erhan Serbest, and Oskar J. Haidn. Turbulent boundary layers with foreign gas transpiration. *Journal of Spacecraft and Rockets*, 38(2):191–198, June 2001.

[30] W. M. Kays. Heat transfer to the transpired turbulent boundary layer. *International Journal of Heat and Mass Transfer*, 15(5):1023–1044, May 1972.

[31] T. Hermann, M. McGilvray, B. Williams, S. Wylie, C. Hambidge, R. Penty-Geraets, A. Bucknell, L. Doherty, and E. Ewart. Total temperature measurements in the oxford high density tunnel. In *AIAA Science and Technology Forum and Exposition*. San Diego, CA, January 2019. submitted.

[32] FG Keyes. A summary of viscosity and heat-conduction data for he, a, h2, o2, co, co2, h2o, and air. *Transactions of the ASME*, 73:589–596, 1951.

[33] F. G. Keyes. The heat conductivity, viscosity, specific heat and prandtl numbers for thirteen gases. Technical Report Project SQUID 37, Massechustetts Institute of Technology Cambridge, 1952.

[34] Christopher J. Roy and Frederick G. Blottner. Review and assessment of turbulence models for hypersonic flows. *Progress in Aerospace Sciences*, 42(7):469–530, October 2006.

[35] R. S. Benson and D. E. Pool. The compressible flow discharge coefficients for a two-dimensional slit. *International Journal of Mechanical Sciences*, 7(5):337–353, May 1965.

[36] Dylan J. Wise and Michael K. Smart. Roughness-induced transition of hypervelocity boundary layers. *Journal of Spacecraft and Rockets*, 51(3):847–854, October 2014.

[37] Andrew N. Ridings. uq's t4 shock tunnel data acquisition system. In *National Instruments Technical Symposium 2012*.

Copyright © 2018 by the author(s)

[38] R. J. Anthony, M. L. G. Oldfield, T. V. Jones, and J. E. LaGraff. Development of high-density arrays of thin film heat transfer gauges. In *5th ASME/JSME Thermal Engineering Joint Conference*, San Diego, CA, March 1999.

[39] M.L.G. Oldfield. Impulse response processing of transient heat transfer gauge signals. *Journal of Turbomachinery*, April 2008.

[40] Rowland T. Penty Geraets, Matthew McGilvray, Benjamin Williams, and Priyav Shah. Laser-based calibration and processing technique for a robust fast-response surface heat transfer gauge. Number 0 in AIAA AVIATION Forum. American Institute of Aeronautics and Astronautics, October 2018.

[41] Matthew Collins, Kam Chana, and Thomas Povey. New technique for the fabrication of miniature thin film heat flux gauges. *Measurement Science and Technology*, 26(2):025303, 2015.

[42] D. L. Schultz and T. V. Jones. *Heat-Transfer Measurements in Short-Duration Hypersonic Facilities*. AGARD, 1973.

[43] G.S. Settles. *Schlieren and Shadowgraph Techniques*. Springer-Verlag Berlin Heidelberg, 2001.

[44] C. Willert, B. Stasicki, J. Klinner, and S. Moessner. Pulsed operation of high-power light emitting diodes for imaging flow velocimetry. *Measurement Science and Technology*, 21(7):075402, 2010.

[45] Nicolas A. Buchmann, Christian E. Willert, and Julio Soria. Pulsed, high-power led illumination for tomographic particle image velocimetry. *Experiments in Fluids*, 53(5):1545–1560, November 2012.

[46] L. M. Weinstein. Review and update of lens and grid schlieren and motion camera schlieren. *The European Physical Journal Special Topics*, 182(1):65–95, April 2010.

[47] Toshinori Kouchi, Christopher P. Goyne, Robert D. Rockwell, and James C. McDaniel. Focusing-schlieren visualization in a dual-mode scramjet. *Experiments in Fluids*, 56(12):211, November 2015.

[48] H. Zare-Behtash, N. Gongora-Orozco, K. Kontis, and S. J. Holder. Application of novel pressure-sensitive paint formulations for the surface flow mapping of high-speed jets. *Experimental Thermal and Fluid Science*, 33(5):852–864, July 2009.

[49] Mark Kenneth Quinn, Leichao Yang, and Konstantinos Kontis. Pressure-sensitive paint: Effect of substrate. *Sensors (Basel, Switzerland)*, 11(PMC3252002):11649–11663, December 2011.

[50] Manuel Guizar-Sicairos, Samuel T. Thurman, and James R. Fienup. Efficient subpixel image registration algorithms. *Opt. Lett.*, 33(2):156–158, January 2008.

[51] Muhammad Hassan Bashir, Chao-Cheng Shiau, and Je-Chin Han. Film cooling effectiveness for three-row compound angle hole design on flat plate using psp technique. *International Journal of Heat and Mass Transfer*, 115:918–929, December 2017.

[52] E. R. Van Driest. Investigation of laminar boundary layer in compressible fluids using the crocco method. Technical Report TN-2597, NACA, 1952.

Copyright © 2018 by the author(s)